Journal of Rock Mechanics and Geotechnical Engineering 18 (2026) 3425–3446

Contents lists available at ScienceDirect

Journal of Rock Mechanics and Geotechnical Engineering

journal homepage: www.jrmge.cn

Full Length Article

Reverse size effect on unconfined compressive strength of red-bed rocks using micro-CT technique

Qinyuan Liang [a], Hengxing Lan [a,b,*], Yu Zhou [c,d,**], Bo Li [e], Shijie Liu [a], Han Bao [f]

[a] College of Geological Engineering and Geomatics, Chang'an University, Xi'an, 710054, China
[b] State Key Laboratory of Resources and Environmental Information System, Institute of Geographic Sciences and Natural Resources Research, Chinese Academy of Sciences, Beijing, 100101, China
[c] Key Laboratory of Rock Mechanics and Geohazards of Zhejiang Province, Shaoxing University, Shaoxing, 312000, China
[d] School of Geoscience and Technology, Southwest Petroleum University, Chengdu, 610500, China
[e] College of Civil Engineering, Tongji University, Shanghai, 200092, China
[f] School of Highway, Chang'an University, Xi'an, 710064, China

ARTICLE INFO

Article history:
Received 14 January 2025
Received in revised form
7 May 2025
Accepted 29 June 2025
Available online 30 July 2025

Keywords:
Red sandstone
Reverse size effect
Unconfined compression test
Pore heterogeneity
Crack propagation
Computed tomography (CT)

ABSTRACT

This study integrates unconfined compression tests with high-resolution computed tomography (CT) to analyze the pore heterogeneity, crack propagation, and failure modes of red sandstone specimens with diameters ranging from 10 mm to 100 mm. Key findings include: (1) With increasing specimen size, crack initiation stress (CI), damage stress (CD), and unconfined compressive strength (UCS) initially increase and then decrease, (2) In smaller specimens, stress concentration due to pore heterogeneity leads to splitting failure and lower strength, (3) In medium-sized specimens, friction dominates crack propagation, causing shear failure, while increased fragment rotation enhances energy dissipation, yielding highest strength, and (4) In larger specimens, cracks tend to propagate along bedding planes, reducing energy dissipation and then weakening strength. These results provide insights into the reverse size effect on sandstone strength and have implications for engineering applications.

1. Introduction

The red-bed rock, predominantly consisting of sandstone and mudstone, is a typical type of sedimentary rock widely distributed in southern China (Rong et al., 2012). One of the primary rock-forming minerals in these rocks is clay minerals, accompanied by varying amounts of ferruginous or calcareous cement. These rocks generally exhibit low cementation strength, well-developed fractures, distinct bedding planes, high porosity, and a tendency to soften when exposed to water (Rong et al., 2012; Liu et al., 2016). Such characteristics make them prone to disintegration and sliding instability (Zhang et al., 2014, 2023; Miščević and Vlastelica, 2019), which can trigger geological disasters such as collapses (McClay et al., 1986), landslides (Zhang et al., 2015), and debris flows (Trümper et al., 2020), as well as engineering issues like foundation instability and deformation or failure of linings and surrounding rocks (Zhang et al., 2024a). In this context, accurately assessing the mechanical properties of red-bed rock masses is of great significance for ensuring engineering safety (Hecht et al., 2005; Yang et al., 2013). Among various mechanical parameters, unconfined compressive strength (UCS) is commonly used due to its simplicity in testing and its effectiveness in directly reflecting the strength characteristics of rock masses (Lan et al., 2010, 2013). Researchers often obtain this parameter through laboratory or field testing (e.g. Han et al., 2022; Liang et al., 2022) and predict strength variations at engineering scales using size effect models (Weibull, 1939, 1951; Bieniawski, 1968; Cuisiat and Haimson, 1992; Bažant, 1984, 1997; Carpinteri et al., 1995; Karakas, 2008; Darlington et al., 2011; Masoumi et al., 2016; Zhai et al., 2020; Liu et al., 2025a, 2025b).

To develop a size effect model, unconfined compression tests on specimens of varying sizes are required. Traditional studies

* Corresponding author. College of Geological Engineering and Geomatics, Chang'an University, Xi'an, 710054, China.
** Corresponding author. Key Laboratory of Rock Mechanics and Geohazards of Zhejiang Province, Shaoxing University, Shaoxing, 312000, China.
E-mail addresses: lanhx@igsnrr.ac.cn (H. Lan), zhouyu@usx.edu.cn (Y. Zhou).
Peer review under responsibility of Institute of Rock and Soil Mechanics, Chinese Academy of Sciences.

https://doi.org/10.1016/j.jrmge.2025.06.014

typically use cylindrical specimens with a standard diameter of 50 mm, covering a size range of 50–2000 mm. The results consistently indicate that UCS decreases progressively with increasing specimen size (Bieniawski, 1968; Cuisiat and Haimson, 1992; Karakas, 2008; Darlington et al., 2011). However, with the growing demand for portable in situ testing, rock specimens with diameters smaller than 50 mm have gained increasing attention (Li et al., 2020; Huang et al., 2020; Qiao et al., 2024). For small-sized specimens, the variation of UCS no longer follows the traditional size effect trend. Instead, UCS initially increases and then decreases as specimen size increases (see Table 1). The initial increase in strength with increasing size is defined as the reverse size effect (Masoumi et al., 2016; Quiñones et al., 2017; Wang et al., 2020). As shown in Table 1, the ascending-descending size effect has been extensively investigated in sedimentary rocks and is recognized as universal.

To explore the causes of the reverse size effect, researchers have investigated multi-scale features such as macroscopic failure modes and microscopic structures. These studies have progressively revealed the critical influence of pore and fracture characteristics, including the spatial distribution, development degree (Ju et al., 2013; Wu et al., 2021), and geometric parameters (Bao et al., 2020; Zhai et al., 2020; Xu, 2022; Zhao et al., 2023a, 2023b). For instance, Jamshidi et al. (2016) demonstrated that the porosity and microcrack density of travertine specimens increase significantly with specimen diameter, profoundly impacting their mechanical behavior. Song et al. (2018) investigated the combined influence of coalbed laminar structure and size effect on UCS anisotropy, revealing a U-shaped variation in strength with loading direction and bedding angle, where increasing size reduced the anisotropy of strength. Similarly, Wu et al. (2021) found that the pore distribution of sandstone becomes more uniform with increasing size, significantly influencing its strength evolution. The influence of internal defect characteristics primarily lies in their ability to alter stress redistribution, thereby directly impacting rock strength, crack initiation paths (He et al., 2024; Wu et al., 2021), and failure modes (e.g. failure morphology, fragmentation degree, and fractal dimensions). Consequently, crack failure characteristics have become an essential basis for uncovering the reverse size effect (Reches, 1999; Tarasov and Potvin, 2013; Barton et al., 2023; González-Fernández et al., 2023, 2024; He et al., 2024; Wu et al., 2021). For example, Liang et al. (2025) investigated the reverse size effect of UCS and its potential controlling factors through unconfined compression tests and numerical simulations. Their findings showed that UCS and failure mode are closely related: as specimen size increases, UCS initially rises monotonically, and failure mode shifts from splitting to shearing. Yang et al. (2023) examined the correlation between size effect (short columns vs. long columns) and rock crack fragmentation, observing that smaller specimens exhibit greater brittleness and higher fragmentation degrees. Zhao et al. (2021) reported that internal defects (e.g. pores and bedding planes) with different spatial scales and forms influence both the size effect and failure characteristics of rocks or rock masses. They emphasized the importance of studying the control mechanisms of defects at varying spatial scales on rock deformation and failure, as well as their impact magnitude. However, existing studies often lack quantitative evaluation and detailed description of fracture characteristics, such as spatial orientation, fragmentation degree, and porosity surrounding defects. This introduces subjectivity into the results and limits a clear understanding of the controlling mechanisms of the reverse size effect in rocks.

To address the limitations, this study took the red sandstone from Ezhou, Hubei Province, China as the research object. A series of unconfined compression tests combined with acoustic emission (AE) techniques was conducted to systematically investigate the reverse size effect and its controlling mechanisms through. Using high-resolution, non-destructive CT technology, the structural characteristics of specimens were meticulously reconstructed in three dimensions before and after fracturing. Based on the precise reconstruction, key parameters, including crack angle distribution, fractal dimensions, fragmentation indices of crack-induced fragments, and the porosity of pores surrounding the cracks were captured and analyzed. This study aims to understand the influence of red sandstone's microstructural features on the reverse size effect, providing essential theoretical insights into the mechanisms of rock engineering disasters.

2. Geological background

The study area is located in Ezhou City, Hubei Province (see Fig. 1), where the red-bed rocks are part of the early Telychian (Lower Silurian) marine siliceous red beds of the Upper Yangtze Platform in South China. Their formation is closely related to the paleoenvironment and tectonic background of that time (Rong et al., 2012; Liu et al., 2016). These red beds are predominantly distributed in shallow marine areas along the margins of ancient continents, with thickness variations depending on their proximity to the ancient landmass. The deposits are thicker near the ancient land and gradually thin out or disappear in more distant areas (Liu et al., 2016). The red beds in the Ezhou region typically have a thickness of several tens of meters. Their reddish color

Table 1
Ascending-descending size effect in sedimentary rocks.

Rock type	Diameter or width (mm)	Aspect ratio	Reverse size effect on strength	Source
Longmont sandstone	25.4–101.6	2:1	Surface defects are the primary cause	Hoskins and Horino (1969)
Kansas limestone	25.4–203.2	2:1	Surface defects are the primary cause	Hoskins and Horino (1969)
Ohya Stone (welded tuff)	30–150	2:1	Fractal distribution of hard particles	Yuki et al. (1995)
Pilton Sandstone	12.5–150	2:1	Presence of weak zone	Hawkins (1998)
Clifton Down limestone	12.5–150	2:1		Hawkins (1998)
Purbeck limestone	12.5–150	2:1		Hawkins (1998)
Pennant sandstone	12.5–150	2:1		Hawkins (1998)
Bath sandstone	12.5–150	2:1		Hawkins (1998)
Burrington Oolite	12.5–150	2:1		Hawkins (1998)
Hollington sandstone	12.5–150	2:1		Hawkins (1998)
Gosford Sandstone	19–145	2:1	Fractal characteristics are the primary mechanism, while surface	Masoumi (2013)
Gosford Sandstone	19–145	2:1	flaws are a secondary mechanism	Masoumi et al. (2016)
Gosford Sandstone	19–145	2:1		Wang et al. (2020)
Gambier limestone	26–285	2:1	End surface flaws are one of the main factors	Zhai et al. (2020)
Sandstone	20–100	2:1	Pore heterogeneity	Wu et al. (2021)

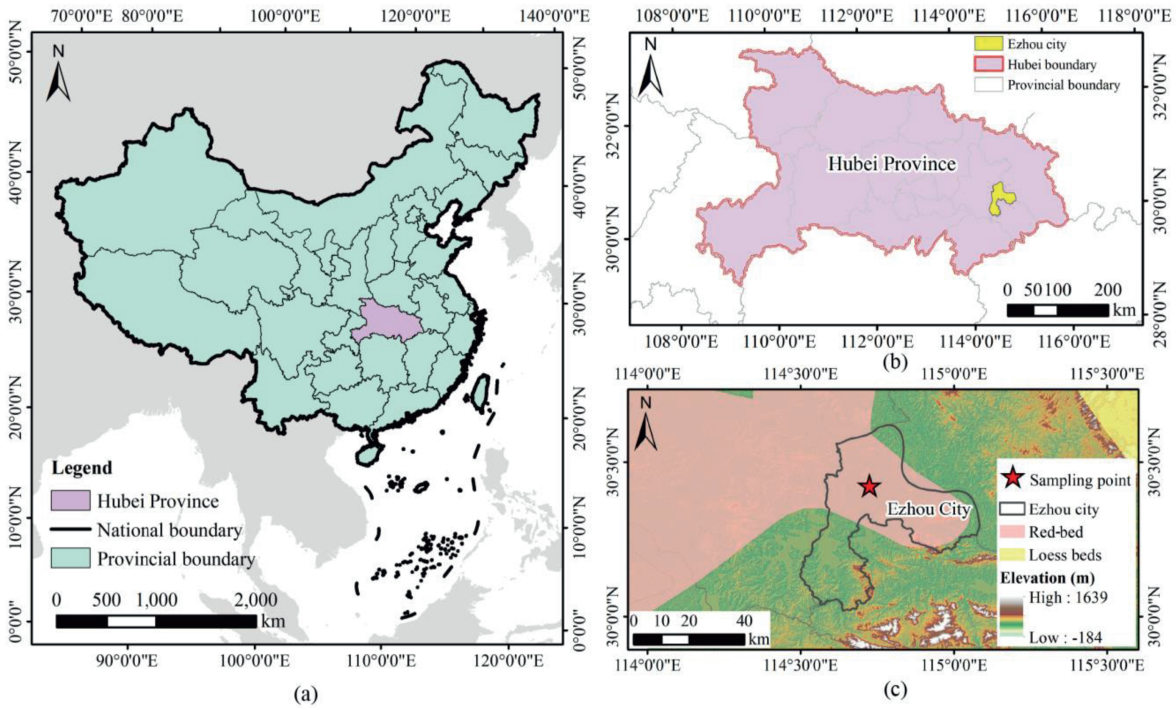

Fig. 1. Location of the study area: (a) Map of China (source: http://bzdt.ch.mnr.gov.cn/index.html); (b) Map of Hubei Province (source: http://bzdt.ch.mnr.gov.cn/index.html); (c) Study area in Ezhou, Hubei Province, with red-bed distribution data from the Open Source Geospatial Foundation (https://www.osgeo.cn/map/mb10c).

originates from iron oxide-rich sediments, which were supplied by adjacent ancient landmasses, such as the Cathaysia Old Land, and transported to shallow marine environments via rivers (Rong et al., 2012; Liu et al., 2016). Furthermore, the region experienced tectonic uplift and fluctuations in sea level during the early Silurian. These tectonic activities not only contributed to the formation of the red beds but also significantly influenced their subsequent engineering properties (Liu et al., 2016).

From an engineering geology perspective, the lithology of the Ezhou red beds primarily consists of fine-grained sandstone, siltstone, and mudstone (Rong et al., 2012; Liu et al., 2016). These rocks are characterized by low hardness and high water-content, making them highly susceptible to weathering under exposure. This weathering often leads to formation of the sliding planes, which may pose significant threats to engineering stability (Ban et al., 2024; Zhang et al., 2024b). Furthermore, the mechanical properties of red sandstone in red-bed areas are closely associated with its lithological characteristics and microstructural features. The distribution of internal defects, such as pores and microcracks, has a critical impact on the overall mechanical behavior of red sandstone. These attributes result in a pronounced strength size effect across specimens of different sizes or engineering scales (Zhang et al., 2014, 2015). Therefore, understanding the size effect of red sandstone is essential for accurately predicting the mechanical behavior of red beds in engineering applications. Such research provides crucial insights for engineering design and stability analysis, contributing to the safe and effective implementation of engineering projects (Wu et al., 2021).

3. Materials and methods

3.1. Materials

Based on a preliminary engineering geological survey, a typical exposed section of red sandstone was selected as the study area, and representative block samples were collected on-site for experimental study. After sampling, the specimens were transported to the laboratory for processing. The samples were first roughly cut and then prepared into cylindrical specimens with diameters of 10 mm, 25 mm, 30 mm, 50 mm, 76 mm, and 100 mm, following the guidelines of the International Society for Rock Mechanics (ISRM, 1979). All specimens were prepared with a height-to-diameter ratio of 2:1. During the preparation process, strict control over geometric precision was maintained to meet the following requirements: the height difference across the same end face was kept within 0.05 mm, the diameter variation along the specimen axis was limited to 0.3 mm, and the tilt angle between the end face and the specimen axis did not exceed 0.25°. To further enhance the surface quality, the top and bottom ends of each specimen were carefully polished.

Subsequently, the mineral composition of the red sandstone is analyzed using X-ray diffraction (XRD) tests (Fig. 2a). The results indicate that the primary mineral components include quartz (64 %), plagioclase (13 %), microcline (6 %), mica (4 %), chlorite (7 %), and calcite (6 %). Microstructural observations (Fig. 2b) reveal that the grain size of the red sandstone ranges from 0.1 mm to 0.25 mm. The cementation characteristics and pore distribution between the grains significantly influence the mechanical properties of the sandstone. Schematic diagrams of specimens with different sizes are presented in Fig. 2c. Considering the higher variability observed in the mechanical testing of small-sized specimens (Masoumi et al., 2016), multiple parallel tests were conducted for each specimen size to ensure the reliability and consistency of the results. The number of specimens prepared for each size is detailed in Table 2.

3.2. Methods

3.2.1. Unconfined tests and AE minoring

To investigate the reverse size effect of compressive strength in

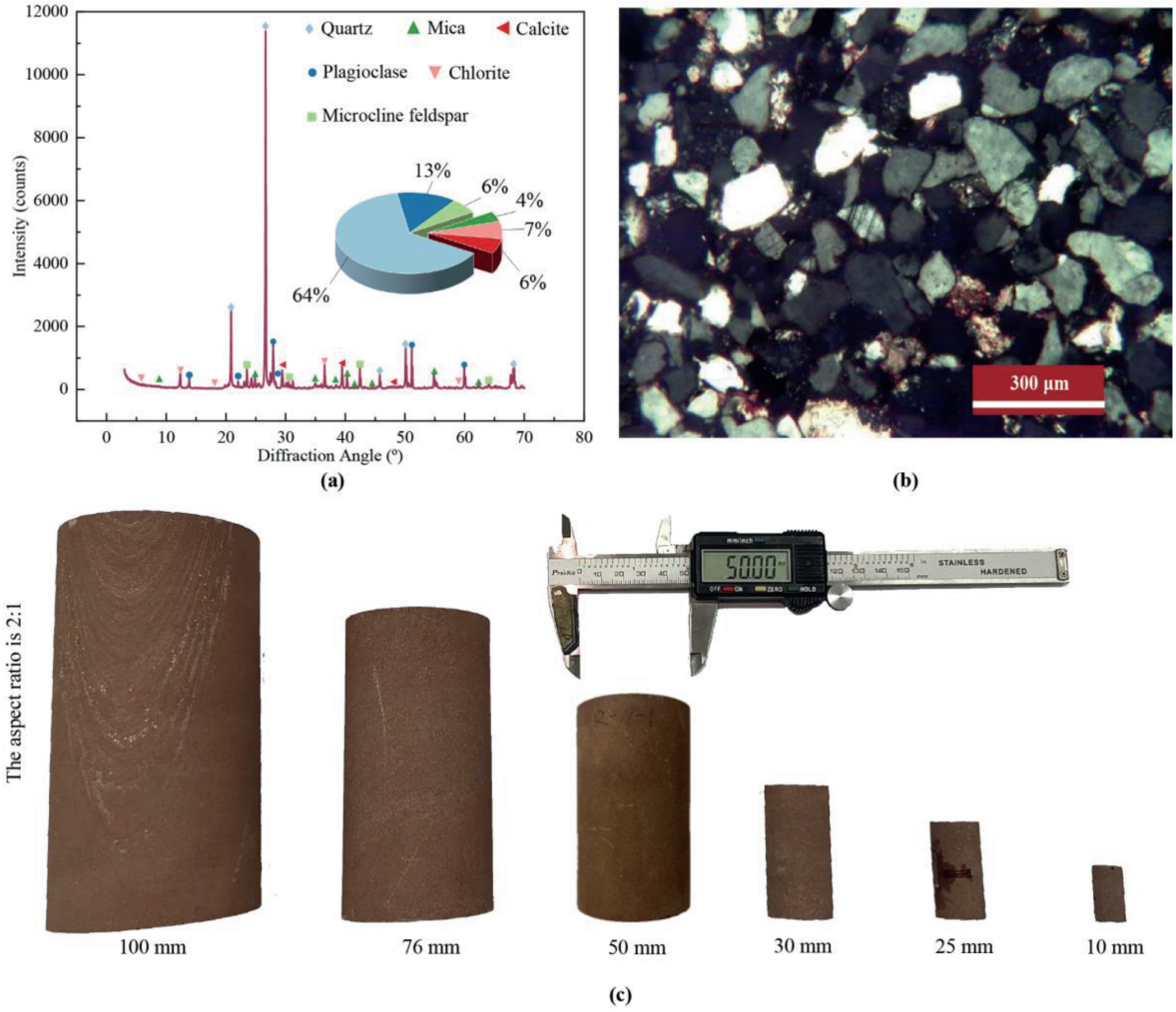

Fig. 2. Characteristics of red sandstone specimens. (a) Mineral composition of red sandstone; (b) Microstructure of red sandstone; (c) Schematic diagrams of red sandstone specimens with different sizes.

rocks, unconfined compression tests are conducted on red sandstone specimens of various sizes using an MTS 815.04 electro-hydraulic servo testing machine (Fig. 3a). The system comprises four main components: a loading control system, a 315-type loading frame, a confining pressure intensifier, and a pore pressure intensifier. In this study, neither confining pressure nor pore pressure was applied. The servo-controller can achieve a maximum axial force of 4600 kN with an accuracy of ±1 %. To minimize end effects that could influence the test results, the top and bottom surfaces of each specimen were uniformly coated with petroleum jelly before formal loading. The mechanical loading was applied in displacement-control mode at a loading rate of 0.001 mm/s. Strain data were collected using a JM3811F strain gauge system, which monitored both lateral and axial strains. The strain gauge has a measurement range of ±19,999 με and a system accuracy of ±0.3 % Fs ± 2 με. The strain acquisition system was synchronized with the mechanical loading system to record data during the entire testing process. The specimens were loaded to failure, at which point loading was stopped, and the test data were exported for further analysis.

Additionally, to monitor the generation and propagation of microcracks within the sandstone specimens during loading, a PAC II acoustic emission (AE) system (manufactured by Physical Acoustics Corporation, AMERICA) was employed and synchronized

Table 2
Sample preparation plan.

Specimen size (mm)	Sample number	Number of samples
$d = 10$, $h = 20$	R10–1, R10–2, R10–3, R10–4, R10–5, R10-6	6
$d = 25$, $h = 50$	R25–1, R25–2, R25–3, R25–4, R25–5, R25-6	6
$d = 30$, $h = 60$	R30–1, R30–2, R30–3, R30–4, R30-5	5
$d = 50$, $h = 100$	R50–1, R50–2, R50-3	3
$d = 76$, $h = 152$	R76–1, R76–2, R76-3	3
$d = 100$, $h = 200$	R100–1, R100–2, R100-3	3

Note: d represents the diameter, and h represents the height.

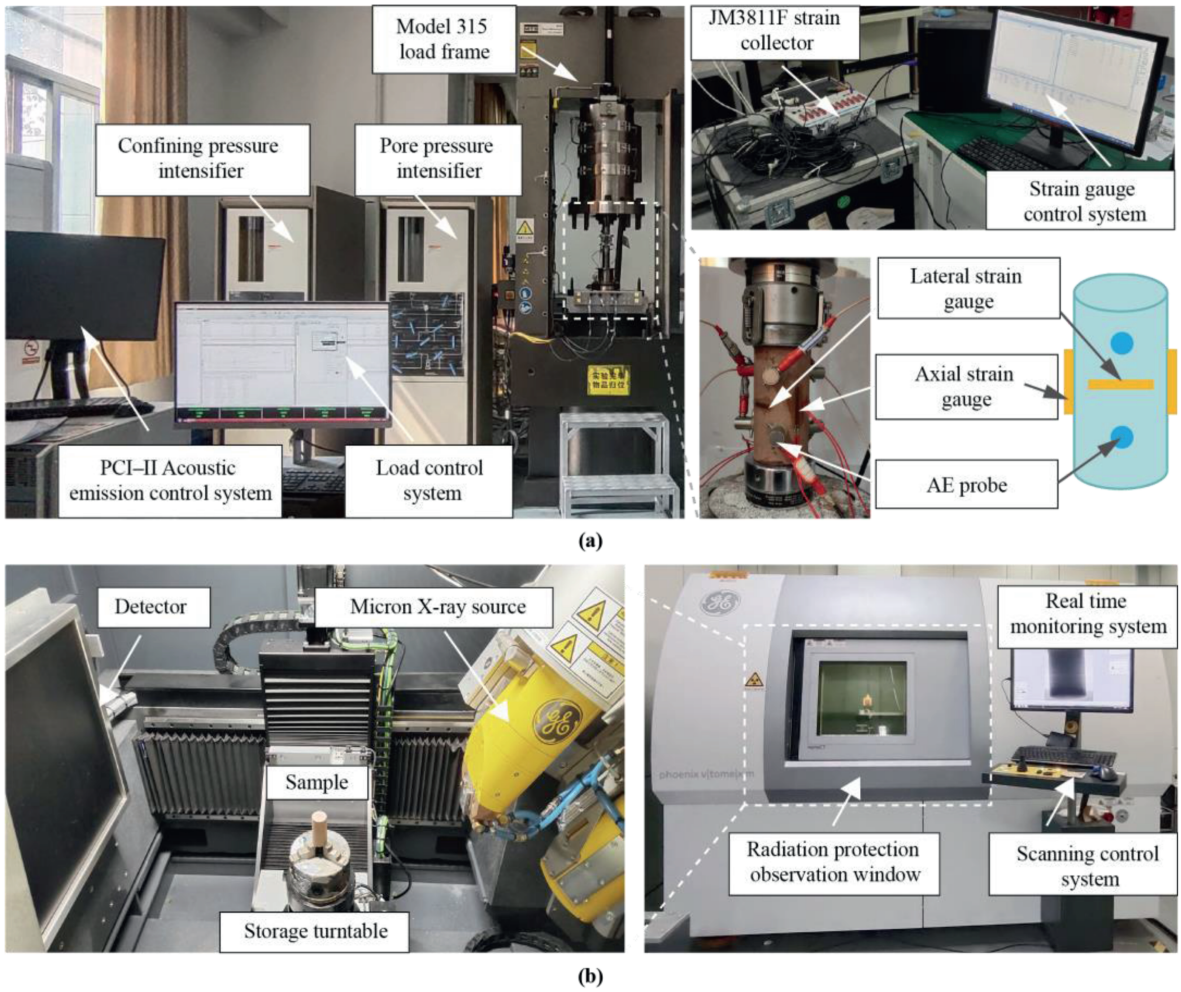

Fig. 3. Experimental equipment for size effect tests. (a) Rock unconfined compression testing system, and (b) Phoenix v|tome|x M micro-CT scanning system.

with the loading system. Six Micro30 sensor probes were evenly distributed along the cylindrical surface of each specimen, operating at a monitoring frequency of 2.5 MHz with a threshold of 40 dB. The AE system was configured to capture real-time information on microcrack initiation and propagation during the loading process, providing critical data to support the analysis of rock failure mechanisms.

3.2.2. X-ray CT

In rock mechanics tests, optical microscopes and scanning electron microscopes (SEM) are commonly used to observe microstructural characteristics (Lan et al., 2019; Qi et al., 2020). However, these methods are limited by a small field of view and lower representativeness, making it difficult to comprehensively display the internal microcrack and pore distribution of rocks. The mechanical response of sandstone is controlled by its internal mineral composition and structure. In particular, pore distribution and crack propagation play a crucial role in revealing the mechanisms underlying the size effect (Hawkins, 1998). High-resolution, non-destructive CT scanning technology provides an effective method for analyzing the internal pore distribution and structural characteristics of sandstone (Wu et al., 2024). Accordingly, in this study we employ a Phoenix V|tome|x M Micro-CT scanner to scan sandstone specimens of varying sizes before and after fracturing (see Fig. 3b). The scanning parameters are as follows: current 150 μA, voltage 150 kV, exposure time 334 ms, rotation step 0.18°, and a total scanning duration of approximately 30 min.

To precisely characterize the microstructural features and microcrack distribution of sandstone, CT images were segmented using thresholding techniques to distinguish different material phases and obtain the three-dimensional (3D) spatial distribution of pores, matrix, and mica within the sandstone. This segmentation and rendering process is illustrated using a 2 mm × 2 mm × 2 mm localized cubic section of sandstone, as shown in Fig. 4. First, the raw CT images are denoised, filtered, and corrected for ring artifacts in turn to enhance image quality and ensure high-resolution 3D reconstructions of the sandstone (Fig. 4a). Based on the relationship between X-ray penetration and sample density, the grayscale probability distribution curve of the sample is obtained (Fig. 4b and c). In the CT grayscale images, high-density regions (e.g. mica and other dense minerals), where X-ray penetration is weaker, appear brighter. Conversely, pores and cracks, due to their lower density and stronger X-ray penetration, appear as darker regions (Zhou et al., 2025a, 2025b). Using morphological features (Yuan et al., 2023), the 3D spatial distribution of pores (Fig. 4d), cracks (Fig. 4e), sandstone matrix (Fig. 4f), and mica (Fig. 4g) are sequentially segmented and identified. The final reconstructed models are shown in Fig. 4h and i, demonstrating a good match between the 3D segmentation results and the original grayscale images. This method effectively enables the refined segmentation of sandstone, providing reliable support for analyzing its internal structural characteristics and crack

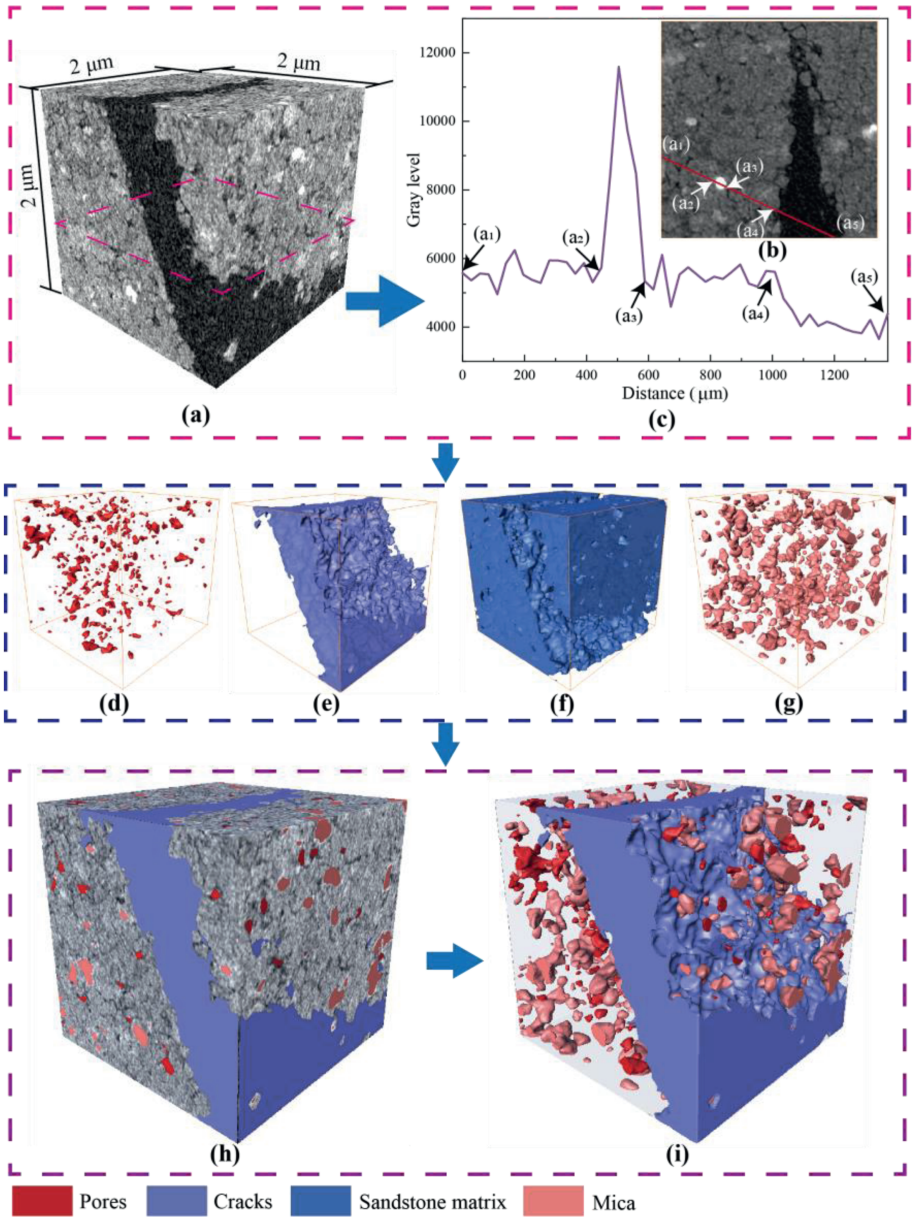

Fig. 4. Material threshold segmentation. (a) 3D grayscale image obtained by X-ray micro-CT, (b) Schematic diagram of a 2D grayscale slice, (c) grayscale probability distribution function corresponding to the 2D grayscale slice, (d) 3D spatial morphology of pores, (e) 3D spatial structure of cracks, (f) 3D spatial structure of the sandstone matrix, (g) 3D spatial morphology of mica, and (h) Rendered 3D compositional model of sandstone; (i) Perspective view of the material after threshold segmentation.

propagation behavior.

4. Results

4.1. Stress-strain curves and mechanical properties

Through mechanical testing, stress-strain curves for specimens of different sizes are obtained, as shown in Fig. 5. It was observed that smaller specimens (with diameters of 10 mm and 25 mm) exhibited more pronounced fluctuations in the stress-strain curves. As the specimen size increased, the curves became progressively smoother, indicating that smaller specimens are more sensitive to local defects and stress heterogeneity. This phenomenon may be attributed to the influence of microstructural irregularities, which plays a more significant role in smaller specimens. In contrast, larger specimens tend to exhibit more uniform mechanical behavior, likely due to the averaging effect of defects over a greater volume. To gain a deeper understanding of the mechanical behavior of sandstone under varying size conditions, it is crucial to analyze the effects of specimen size on crack initiation stress (CI), damage stress (CD), and UCS (Quiñones et al., 2017). Specifically, CI can be determined from the crack volumetric strain - axial strain curve, while CD can be obtained from the total volumetric strain - axial strain curve, as shown in Fig. 6.

The total volumetric strain (ε_v) and crack volumetric strain (ε_v^c) are respectively (Martin and Chandler, 1994):

$$\varepsilon_v = \frac{\Delta V}{V} \approx \varepsilon_{axial} + 2\varepsilon_{lateral} \quad (1)$$

Where ΔV denotes the change in volume of the sample during the loading process, while V represents the initial volume of the rock

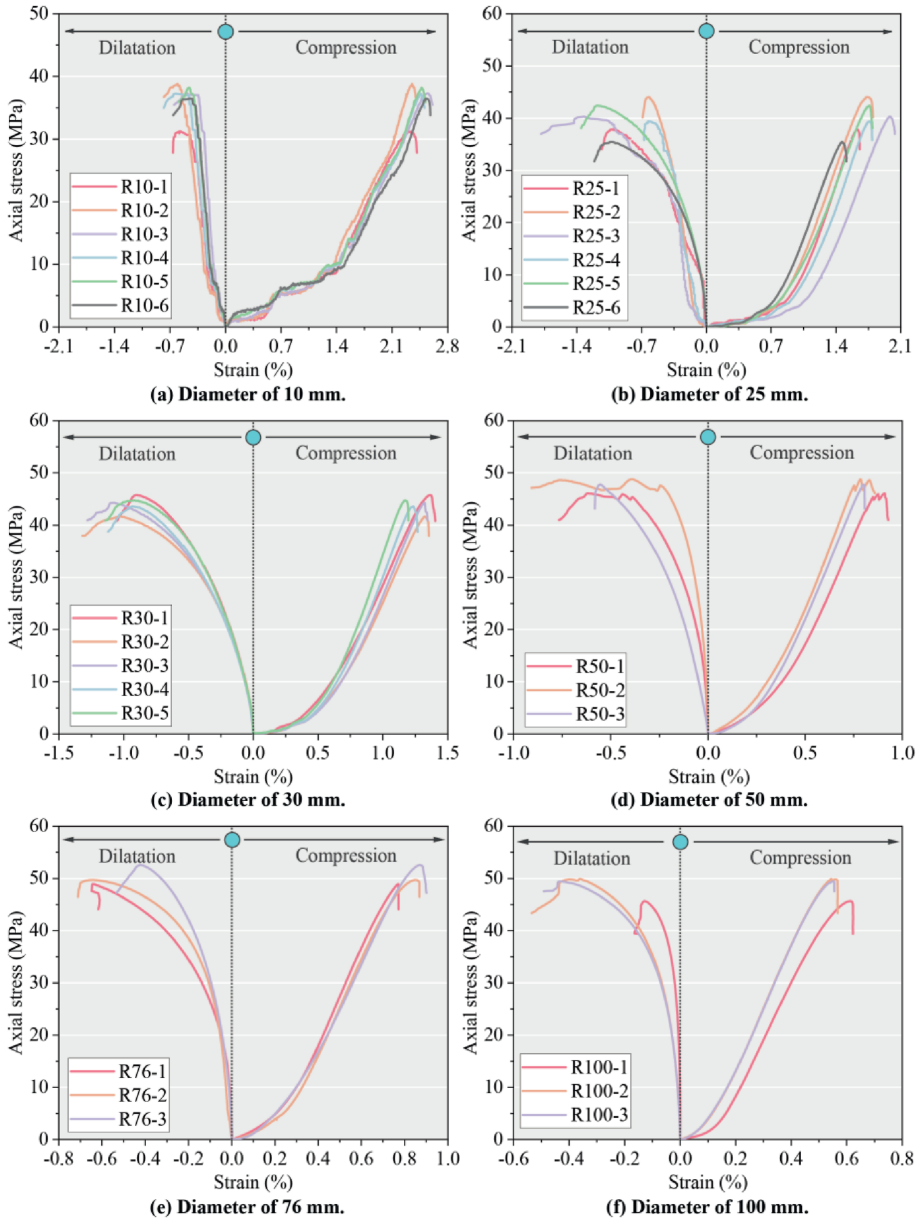

Fig. 5. Stress-strain curves of specimens with different sizes. (a) Diameter of 10 mm; (b) Diameter of 25 mm; (c) Diameter of 30 mm; (d) Diameter of 50 mm; (e) Diameter of 76 mm; (f) Diameter of 100 mm.

sample before deformation. The terms $\varepsilon_{\text{axial}}$ and $\varepsilon_{\text{lateral}}$ refer to the axial and lateral strains, respectively. The crack volumetric strain ($\varepsilon_{\text{v}}^{\text{c}}$) is determined by subtracting the elastic volumetric strain ($\varepsilon_{\text{v}}^{\text{e}}$) from the total volumetric strain:

$$\varepsilon_{\text{v}}^{\text{c}} = \varepsilon_{\text{v}} - \varepsilon_{\text{v}}^{\text{e}} \tag{2}$$

The elastic volumetric strain is calculated based on linear elasticity:

$$\varepsilon_{\text{v}}^{\text{e}} = \frac{1-2\nu}{E}\sigma \tag{3}$$

where E is the elastic modulus, ν is the Poisson's ratio, and σ is the axial stress under unconfined compression.

The elastic modulus and Poisson's ratio are determined from the linear segment of the stress-strain curve. The elastic modulus is calculated as

$$E = \frac{\sigma_b - \sigma_a}{\varepsilon_{lb} - \varepsilon_{la}} \tag{4}$$

$$\upsilon = \frac{\varepsilon_{db} - \varepsilon_{db}}{\varepsilon_{lb} - \varepsilon_{la}} \tag{5}$$

where E is the average elastic modulus of the rock (GPa), σ_b is the axial stress at the endpoint of the linear segment on the stress-strain curve (MPa), and σ_a is the axial stress at the start point of the linear segment on the stress-strain curve (MPa). ε_{lb} represents the axial strain corresponding to σ_b, and ε_{la} represents the axial strain corresponding to σ_a. Additionally, υ denotes the average Poisson's ratio of the rock, ε_{db} is the lateral strain corresponding to σ_b, and ε_{da} is the lateral (radial) strain corresponding to σ_a.

After calculation, the strength parameters and their variation with specimen size are presented in Fig. 7. The results show that as

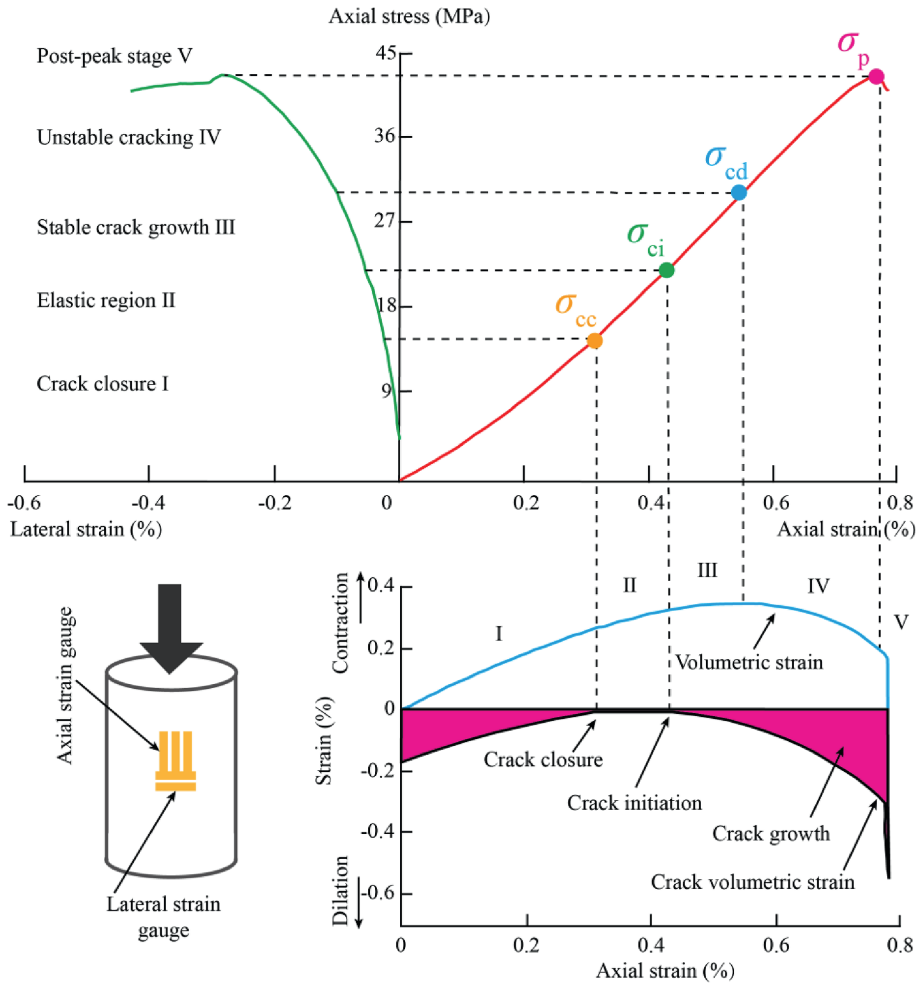

Fig. 6. Stress-strain curve and strength characteristic point determination (modified from Martin and Chandler, 1994).

the specimen diameter increases from 10 mm to 76 mm, CI, CD, and UCS exhibit a significant increase, with UCS showing the most pronounced growth—an average increase of 37.80 %. This trend indicates that within a certain range, increasing specimen size enhances the compressive performance of sandstone. The abrupt increase in strength between 25 mm and 30 mm may be attributed to the inherent heterogeneity and dispersion of small-sized specimens. However, when the diameter further increases from 76 mm to 100 mm, UCS begins to decline, with an average reduction of 14.37 %. This trend aligns with the traditional size effect, where strength decreases with larger specimens, due to an increased prevalence of internal weak planes (Zhang et al., 2011; Zhao et al., 2022, 2023b; Zhou et al., 2024). In contrast, CI and CD remain relatively stable within this range, showing minimal size dependency. These findings are consistent with trends reported in previous studies (e.g. Yuki et al., 1995; Hawkins, 1998; Darlington et al., 2011; Masoumi et al., 2016; Quiñones et al., 2017; Zhai et al., 2020; Wu et al., 2021) and further support the observed reverse size effect in rock mechanics.

Given the significant differences in stress values across specimens of different sizes, crack initiation stress (CI) and damage stress (CD) are normalized against UCS (CI/UCS and CD/UCS) to more effectively compare their relative contributions to the failure process (Quiñones et al., 2017), as shown in Fig. 8. The results indicate that the normalized crack initiation stress (CI/UCS) and normalized damage stress (CD/UCS) exhibit a trend of initially

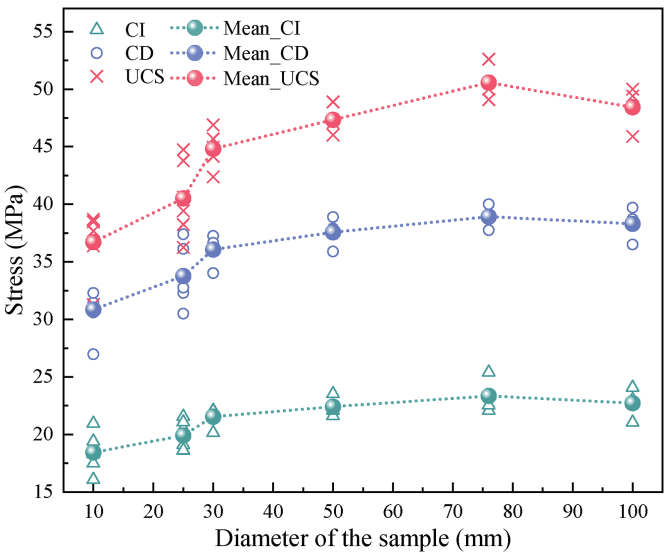

Fig. 7. Effects of size effect on mechanical parameters.

decreasing and then increasing with increasing specimen size. Specifically, as the specimen diameter increases from 10 mm to 76 mm, the average CI/UCS decreases from 0.503 to 0.461,

representing a reduction of 8.35 %, while the average CD/UCS decreases from 0.842 to 0.769, corresponding to a reduction of 8.67 %. However, when the specimen diameter increases from 76 mm to 100 mm, the average CI/UCS increases from 0.461 to 0.469, with a growth of 1.74 %, and the average CD/UCS increases from 0.769 to 0.791, reflecting an increase of 2.86 %. This trend indicates that as the specimen size increases, the crack initiation and damage processes exhibit different characteristics, thereby affecting the progressive failure of the rock.

AE technology is capable of monitoring crack initiation and propagation in real time (Su et al., 2023). In this study, the variation of the cumulative AE ringing response with normalized time was analyzed, and the spatiotemporal evolution of cracks in specimens of different sizes is compared, as shown in Fig. 9. Overall, small-sized specimens (diameters of 10 mm and 25 mm) exhibit distinct brittle failure characteristics. Their axial stress undergoes instability failure at relatively low levels, and AE activity rapidly increases within a short period before failure. This indicates that cracks remain relatively stable for a long time until stress reaches a threshold, at which point they suddenly propagate, leading to instantaneous failure. As the specimen size increases (diameters of 30 mm, 50 mm, and 76 mm), the initiation time of AE activity advances, and the accumulation rate tends to flatten, reflecting the progressive nature of crack propagation and damage evolution. That is, cracks begin to propagate at lower stress levels and undergo a prolonged damage accumulation phase. Notably, when the specimen diameter further increases to 100 mm, the AE release pattern changes, and its accumulation rate tends to surge, indicating that the progressive failure characteristics weaken to some extent.

To reveal the effect of size on deformation parameters, the elastic modulus and Poisson's ratio of specimens with different sizes were calculated using Eqs. (4) and (5) (as shown in Fig. 10). From the figure, it can be observed that the elastic modulus increases significantly with specimen size, with its average value rising from 2.80 GPa to 11.91 GPa, representing an increase of 325.36 %. Larger specimens exhibit higher elastic modulus values, indicating that sandstone demonstrates greater resistance to deformation during the compression process. These results are consistent with previous studies (e.g. Quiñones et al., 2017; Li et al., 2018; Wu et al., 2021). In contrast, Poisson's ratio shows a fluctuating trend with increasing specimen size, ranging between 0.10 and 0.25, without a clear monotonic pattern. This observation aligns with findings from earlier research (Quiñones et al., 2017; Zhai et al., 2020).

4.2. Quantitative analysis of pore and fracture structures

In the previous section, the mechanical properties and deformation characteristics of sandstone specimens with different sizes were analyzed. The mechanical and deformation behaviors are closely related to the pore distribution and failure characteristics within the specimens (He et al., 2024; Wu et al., 2021). Therefore, understanding the role of the spatial distribution of natural pores in crack propagation is crucial. However, due to the complexity of pore spatial distribution and crack propagation paths, traditional experimental methods face challenges in accurately capturing these microstructural features (Chen et al., 2018; Liu et al., 2023, 2024). To address this, this section analyzes the spatial distribution of pores, crack failure morphologies, fractal dimensions of cracks, characteristics of crack-induced fragments, and the influence of surrounding pores on the size effect using CT scan images of specimens with different sizes. For each specimen size, three parallel samples are examined to ensure the reliability and consistency of the analysis. This approach aims to uncover the mechanisms by which pore distribution affects crack propagation from a microstructural perspective.

4.2.1. Spatial characteristics of pores

Fig. 11 presents the initial pore distribution (left) and the 3D visualization of primary cracks after failure (right) for sandstone specimens of varying sizes. Based on CT scan results, it is evident that small-sized specimens (diameters of 10 mm and 25 mm) exhibit significant heterogeneity in pore spatial distribution. As the specimen size increases, the pore distribution becomes progressively more uniform. The spatial heterogeneity decreases markedly, particularly in the specimen with a diameter of 76 mm, where the pore distribution appears relatively consistent, and variations in pore volume are minimal, indicating high pore structure homogeneity. Although other specimens (with diameters ranging from 10 mm to 76 mm) may exhibit some localized layered structures, in the 100 mm diameter specimen, the pore distribution is significantly influenced by bedding planes, displaying a distinct, large, and continuous layered structure, which is more pronounced compared to other sizes.

Quantifying the spatial heterogeneity of pores in sandstone specimens presents significant challenges in experiments (Lan et al., 2010; Nicksiar and Martin, 2014; Peng et al., 2017). To address this, the concept of entropy was introduced to quantify the spatial irregularity of pore distributions (Xu et al., 2020; Cheng et al., 2022; Han et al., 2023). Specifically, entropy is used to

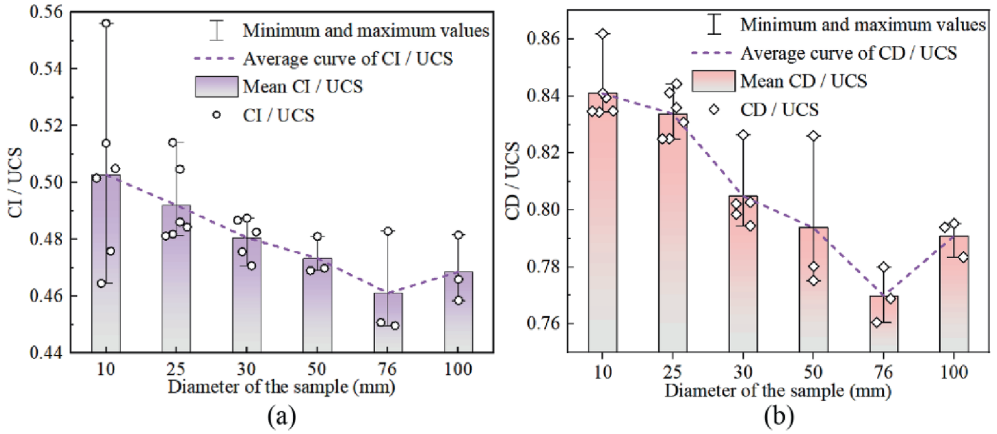

Fig. 8. Normalized characteristic stress thresholds of specimens with different sizes: (a) Normalized crack initiation stress (CI/UCS), and (b) normalized crack damage stress (CD/UCS).

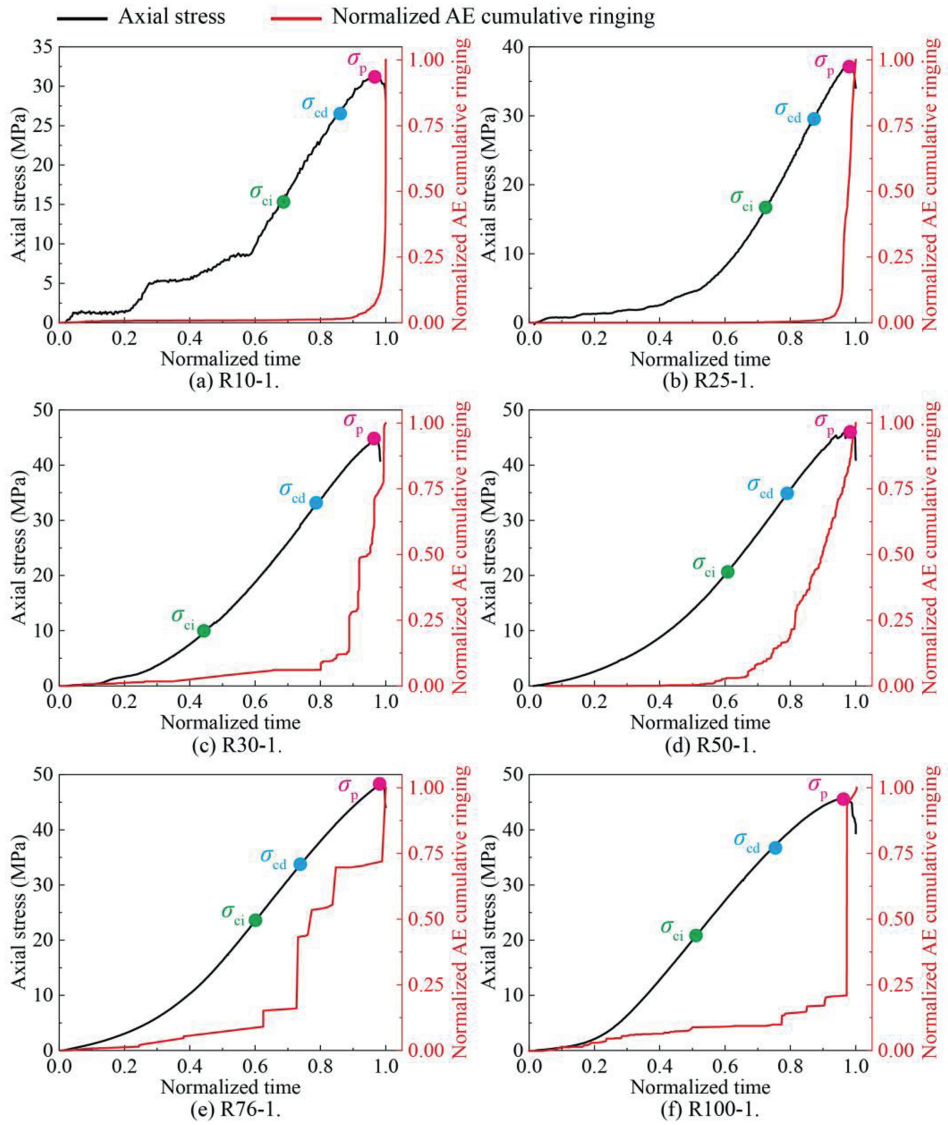

Fig. 9. Evolution of axial stress and AE activity for specimens of different sizes. (a) Specimen R10-1, (b) Specimen R25-1, (c) Specimen R30-1, (d) Specimen R50-1, (e) Specimen R76-1, and (f) Specimen R100-1.

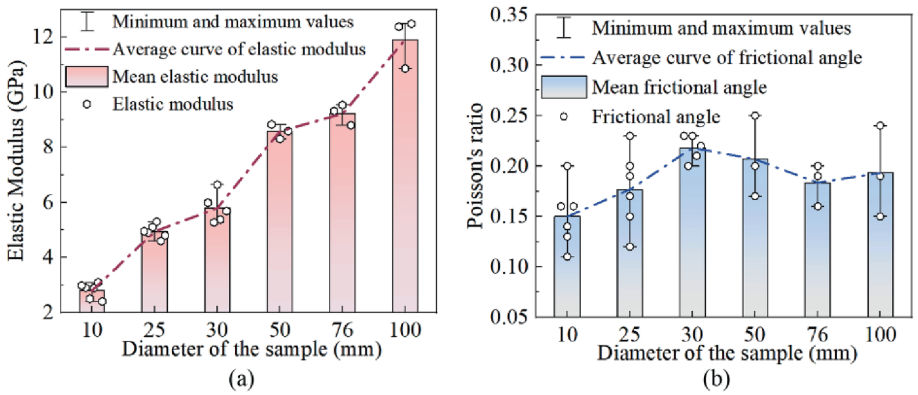

Fig. 10. Effects of size effect on deformation parameters. (a) Elastic modulus, and (b) Poisson's ratio.

describe the degree of disorder in 3D spatial distribution of pores. A higher entropy value indicates a more disordered and uniform distribution of pores, whereas a lower entropy value signifies a more concentrated and ordered distribution.

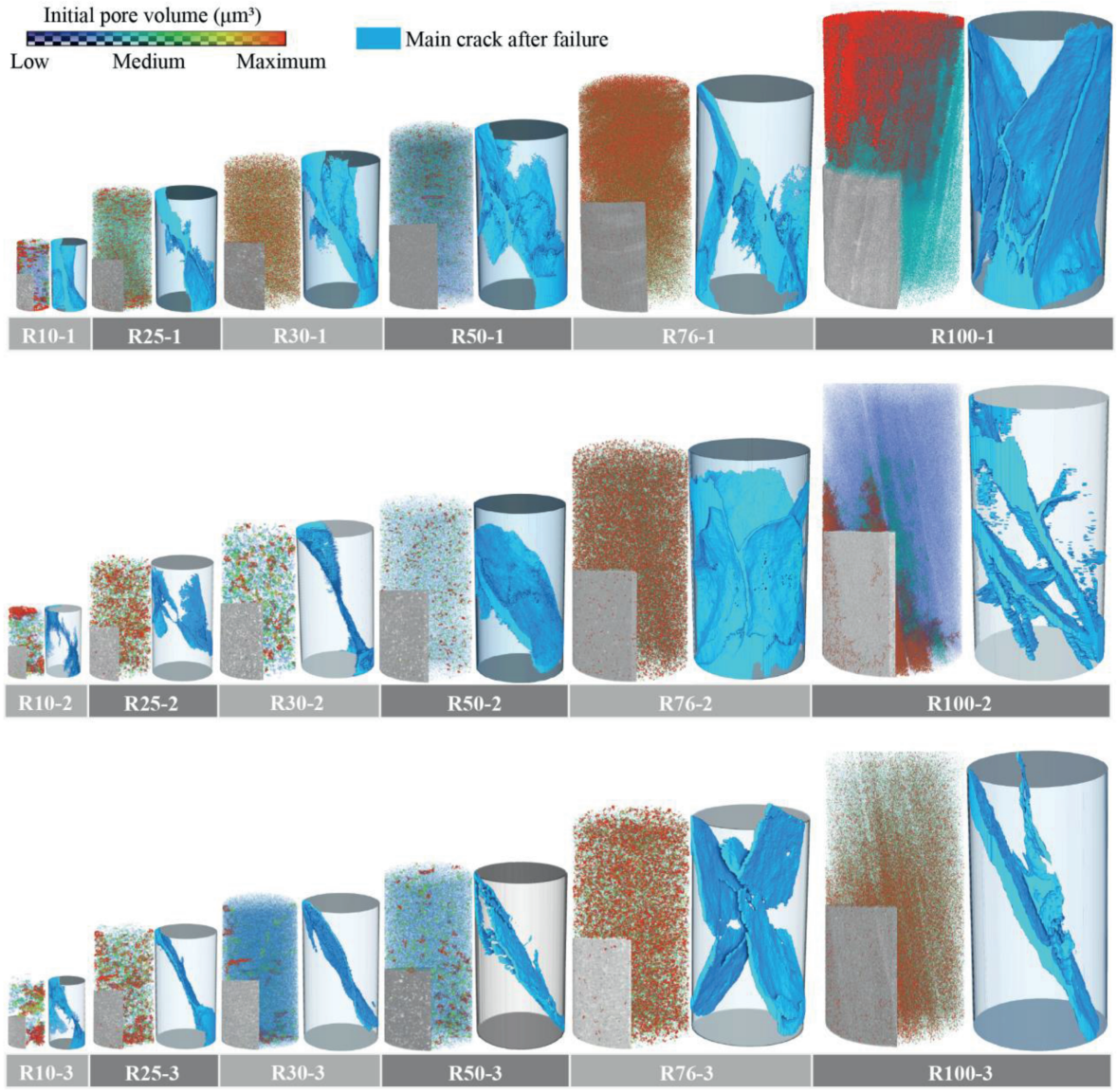

Fig. 11. CT scan results. Initial pore distribution for specimens of different sizes (left) and 3D visualization of primary cracks in fractured specimens of different sizes (right).

The calculation of entropy involves the following steps:

(1) Division of the 3D grid: The 3D volume of the specimen is divided into multiple equal-volume grid cells. Based on the range of *X*, *Y*, and *Z* coordinates, the grid is divided into 200, 200, and 400 cells along the respective axes, ensuring that the detailed spatial variation of pores is captured adequately.
(2) Calculation of pore volume for each grid cell: Using the 3D coordinates of pore points, the corresponding grid cells are identified, and the pore volume within each cell is accumulated.
(3) Compute the volume fraction for each grid cell: Normalize the pore volume of each grid cell by dividing it by the total volume of the specimen, obtaining the volume fraction p_i.

Based on p_i, the pore spatial heterogeneity entropy of the sandstone specimen is calculated using:

$$H = -\sum_i p_i \log_{10} p_i \tag{6}$$

where H represents the pore spatial heterogeneity entropy, and p_i represents the volume fraction of the i-th grid cell.

Fig. 12 presents the average entropy values of the initial pore spatial heterogeneity for sandstone specimens with different sizes. As the specimen diameter increases from 10 mm to 76 mm, the average entropy rises from 9.18 to 13.74, representing an increase of 49.67 %. This indicates that with increasing specimen size, the uniformity of pore distribution improves, and spatial heterogeneity gradually decreases. However, when the specimen diameter further increases to 100 mm, the entropy drops sharply from 13.74 to 7.40, marking a decrease of 46.14 %. This abrupt decline in entropy suggests that in larger specimens, pore distribution is significantly influenced by the bedding planes of sandstone, where pores become more interconnected along bedding planes (Fig. 11), leading to a more concentrated and orderly spatial distribution. For specimens with diameters ranging from 10 mm to 76 mm, the

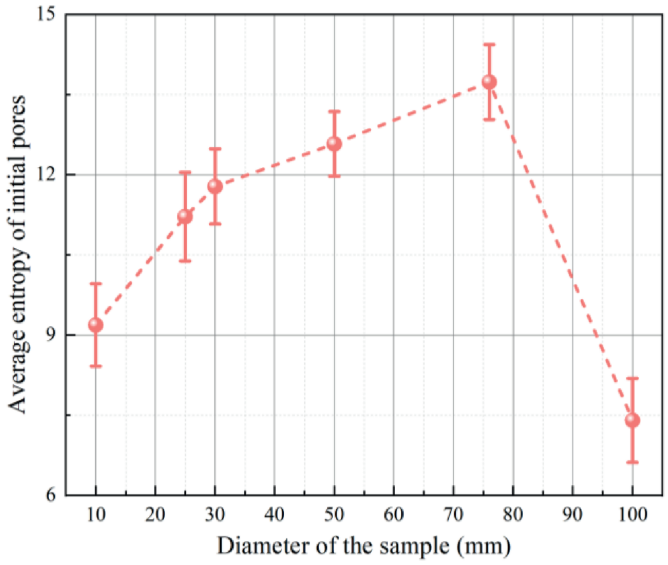

Fig. 12. Average entropy of initial pores in specimens of different sizes.

relatively small size may not be sufficient to fully capture continuous bedding structures, and therefore, the distribution is primarily influenced by the initial heterogeneity of pore space. In contrast, the 100 mm specimens are large enough to contain intact bedding planes, which lead to the alignment of pores along these planes, and thus the larger specimens are primarily influenced by the bedding distribution. Therefore, the average entropy of initial pores can reflect the heterogeneity of the pore space distribution. The pore space heterogeneity is larger in small-sized specimens, and as the specimen size increases to medium sizes, the pore space becomes more uniform. However, in large-sized specimens, the influence of bedding planes becomes evident, causing the pore space distribution to present a distinct layered structure along the bedding planes.

4.2.2. Relationship between fracture angle range and failure mode

Analyzing crack propagation paths and failure modes is crucial for understanding the size effect in rocks (González-Fernández et al., 2023, 2024). Fig. 13 presents the physical images of the failure modes of specimens of different sizes. However, solely analyzing the surface cracks makes it challenging to infer the distribution of internal cracks (Chen et al., 2018; Liu et al., 2023). To address this, CT scanning technology is employed to capture the 3D crack morphology of fractured specimens of varying sizes, as shown in Fig. 11. Overall, the failure mode of small-sized specimens primarily exhibits a combination of localized splitting and shear failure. As the specimen size increases, shear failure progressively becomes dominant. Specifically, in small-sized specimens (diameters of 10 mm, 25 mm, and 30 mm), localized splitting failure is concentrated in regions with dense pore distributions, while shear failure dominates in other areas. This indicates that the spatial distribution of pores has a significant influence on crack paths in small-sized specimens. As the specimen size increases to 50 mm and 76 mm, the pore distribution becomes more uniform, and the effect of pore heterogeneity on crack propagation paths gradually diminishes. Shear failure increasingly dominates the crack propagation process. For specimens with a diameter of 100 mm, crack propagation develops along bedding planes, exhibiting tensile-shear composite failure characteristics, with shear failure as the dominant mode accompanied by localized tensile failure. This transition in failure modes reflects the significant enhancement of bedding effects in larger specimens, which influences crack propagation paths and failure mechanisms.

The propagation direction of cracks in 3D space is highly complex and variable. Traditional methods are mostly qualitative, and precise quantitative descriptions remain a significant challenge (Ramsey and Chester, 2004; González-Fernández et al., 2023). However, quantifying the angular distribution of cracks not only allows for distinguishing whether tensile or shear failure is dominant and identifying their relative proportions but also more accurately reveals the spatial characteristics of crack propagation. To achieve a quantitative analysis of the propagation direction of cracks in sandstone specimens, this study utilizes a custom-developed program to calculate the angular distribution of cracks.

(1) Extraction of normal vectors

First, high-precision 3D geometric models of the specimens were generated using 3D data processing software. These models are composed of multiple triangular facets that accurately describe the geometric features of the cracks. Each triangular facet is defined by three vertices $\overrightarrow{V_1}, \overrightarrow{V_2}, \overrightarrow{V_3}$, and the normal vector $\overrightarrow{n}$ can be calculated using the cross-product formula as follows:

$$\overrightarrow{n} = \left(\overrightarrow{V_2} - \overrightarrow{V_1}\right) \times \left(\overrightarrow{V_3} - \overrightarrow{V_1}\right) \tag{7}$$

where $\overrightarrow{V_1}, \overrightarrow{V_2}, \overrightarrow{V_3}$ represent the coordinates of the three vertices of the triangular facet; and $\overrightarrow{n}$ is the normal vector of the facet, indicating its orientation and position in 3D space.

(2) Calculation of the angle between the normal vector and *Z*-axis

To accurately determine the propagation direction of cracks, it is necessary to calculate the angle θ between the normal vector $\overset{n}{\rightarrow}$ of each triangular facet and *Z*-axis $\overset{z}{\rightarrow} = (0, 0, 1)$. The calculation formula is as follows:

$$\theta = \arccos\left(\frac{\overrightarrow{n} \cdot \overrightarrow{z}}{|\overset{n}{\rightarrow}|}\right) \tag{8}$$

where $\overset{n}{\rightarrow} \cdot \overset{z}{\rightarrow} = n_z$ represents the *Z*-component of the normal vector, and $|\overset{n}{\rightarrow}|$ is the magnitude of the normal vector as

$$|\overset{n}{\rightarrow}| = \sqrt{n_x^2 + n_y^2 + n_z^2} \tag{9}$$

where n_x, n_y, n_z denote the components of the normal vector $\overset{n}{\rightarrow}$ along the *X*-axis, *Y*-axis, and *Z*-axis, respectively. This formula calculates θ, the angle between the normal vector of each facet and the specimen axis (*Z*-axis), by using the dot product and magnitude of the vectors. This angle represents the geometric characteristics of the crack propagation direction.

(3) Statistical analysis of crack angle distribution

To quantitatively describe the characteristics of the crack angle distribution, the following formula is used to calculate the frequency distribution of crack angles:

$$f(\theta) = \frac{N_\theta}{N_{\text{total}}} \tag{10}$$

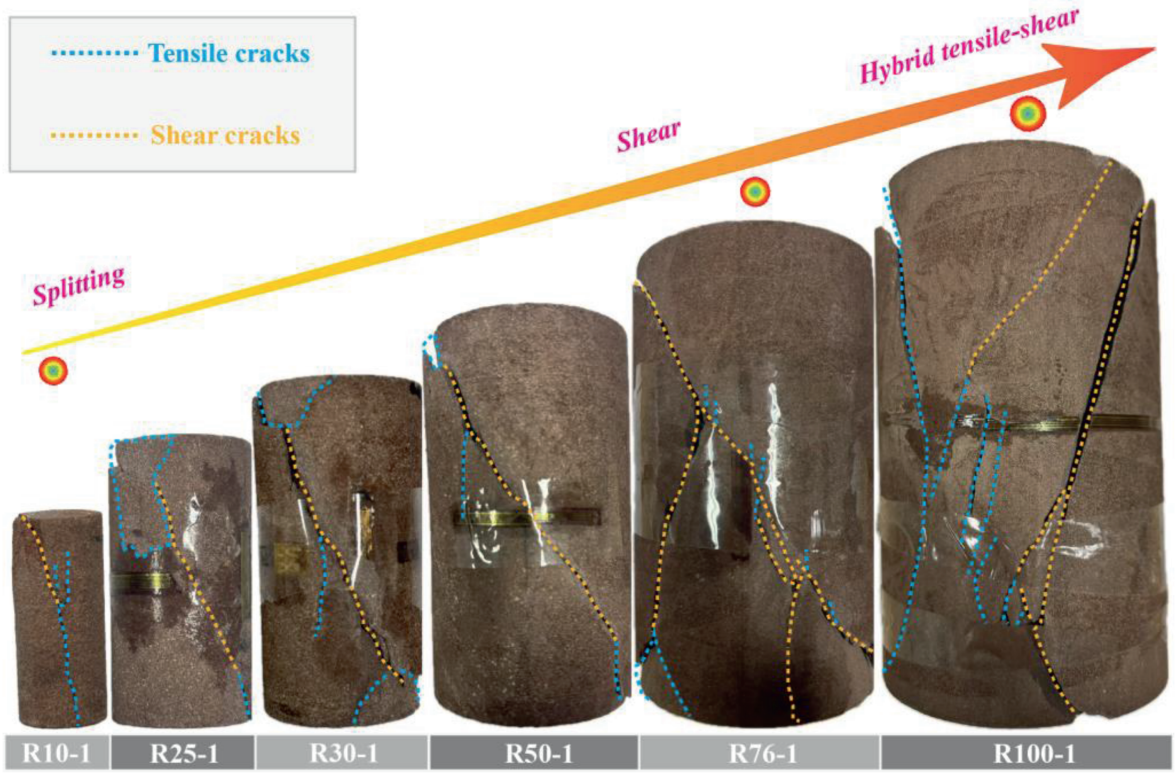

Fig. 13. Failure modes of red sandstone with different sample sizes under unconfined compression.

where N_θ represents the number of cracks with an angle of θ, and N_{total} is the total number of cracks. This frequency distribution function visually reveals the characteristics of the crack angle distribution, facilitating further analysis of the spatial inclination of crack propagation.

Based on the above method for calculating the crack angle distribution, the crack angle distribution patterns for sandstone specimens of different sizes are obtained, as shown in Fig. 14. To better correlate with the analysis of crack angles, *RA* (rise angle) and *AF* (average frequency) are calculated from AE signals to characterize the tensile and shear properties of cracks (Shiotani et al., 2001; Ohno and Ohtsu, 2010; Aggelis, 2011; Wang et al., 2016), as shown in Fig. 15.

Observing Fig. 14, Rd-1, Rd-2, and Rd-3 represent three parallel specimens. For each subplot, the horizontal axis represents the crack angle, while the vertical axis indicates the number of triangular faces within the corresponding angle range. For small specimens (10 mm, 25 mm, and 30 mm), the crack angles are primarily concentrated between 75° and 105°, indicating that tensile failure predominates. However, as the specimen size increases (50 mm, 76 mm), the crack angle distribution broadens significantly, suggesting that shear failure increasingly influences the failure mechanism, with the crack angle range extending from 50° to 130°. For large specimens (100 mm), the crack angles again concentrate between 75° and 105°, and the crack propagation is highly aligned with the loading direction, showing a mixed tensile-shear failure mode. The AE signal analysis in Fig. 15 further confirms this trend. For small specimens, AE data points are mainly concentrated in the region with low *RA* values and high *AF* values, indicating tensile failure dominance. As the specimen size increases (50 mm, 76 mm), AE data points gradually move towards the region with high *RA* values and low *AF* values, highlighting the increasing influence of shear failure. For large specimens (100 mm), AE data points shift back to the region with low *RA* values and high *AF* values, indicating that tensile failure again dominates. Therefore, the frequency distribution of crack angles is validated by the AE signal, reflecting the angular distribution of 3D cracks. The failure mechanism transitions from a combination of splitting and shear failure in small specimens to predominantly shear failure in medium-sized specimens, and eventually to a mixed tensile-shear failure mode in large specimens.

4.2.3. Fractal dimension of fractures

The geometric complexity and spatial self-similarity of cracks are the key to understand the material fracture behavior (Barton et al., 2023). However, relying solely on traditional geometric parameters (e.g. length, width, and area) makes it challenging to fully reveal the microstructural details and irregularities of crack structures (Rahner et al., 2018). To address this, the fractal dimension is introduced as a descriptor tool to quantitatively capture the intricate details and self-similarity of cracks. The fractal dimension is calculated using the classical box-counting method. The specific approach involves varying the grid size e, counting the number of grid cells $\ln(N(e))$ that the crack structure covers, plotting the relationship between $\ln(N(e))$ and $\ln(N(1/e))$ (Russell et al., 1980; Wang et al., 2019), and performing a least-squares linear fit. The fractal dimension D is determined by

$$D = \lim_{e \to 0} \frac{\ln(N(e))}{\ln(1/e)} \tag{11}$$

The results of the 3D fractal dimension of cracks, shown in Fig. 16, represents the average values for different sample diameters. It can be observed that as the sample diameter increases, the 3D fractal dimension of the cracks first increases and then decreases, indicating a clear positive correlation with the strength size effect. Specifically, for the smallest sample diameter (10 mm),

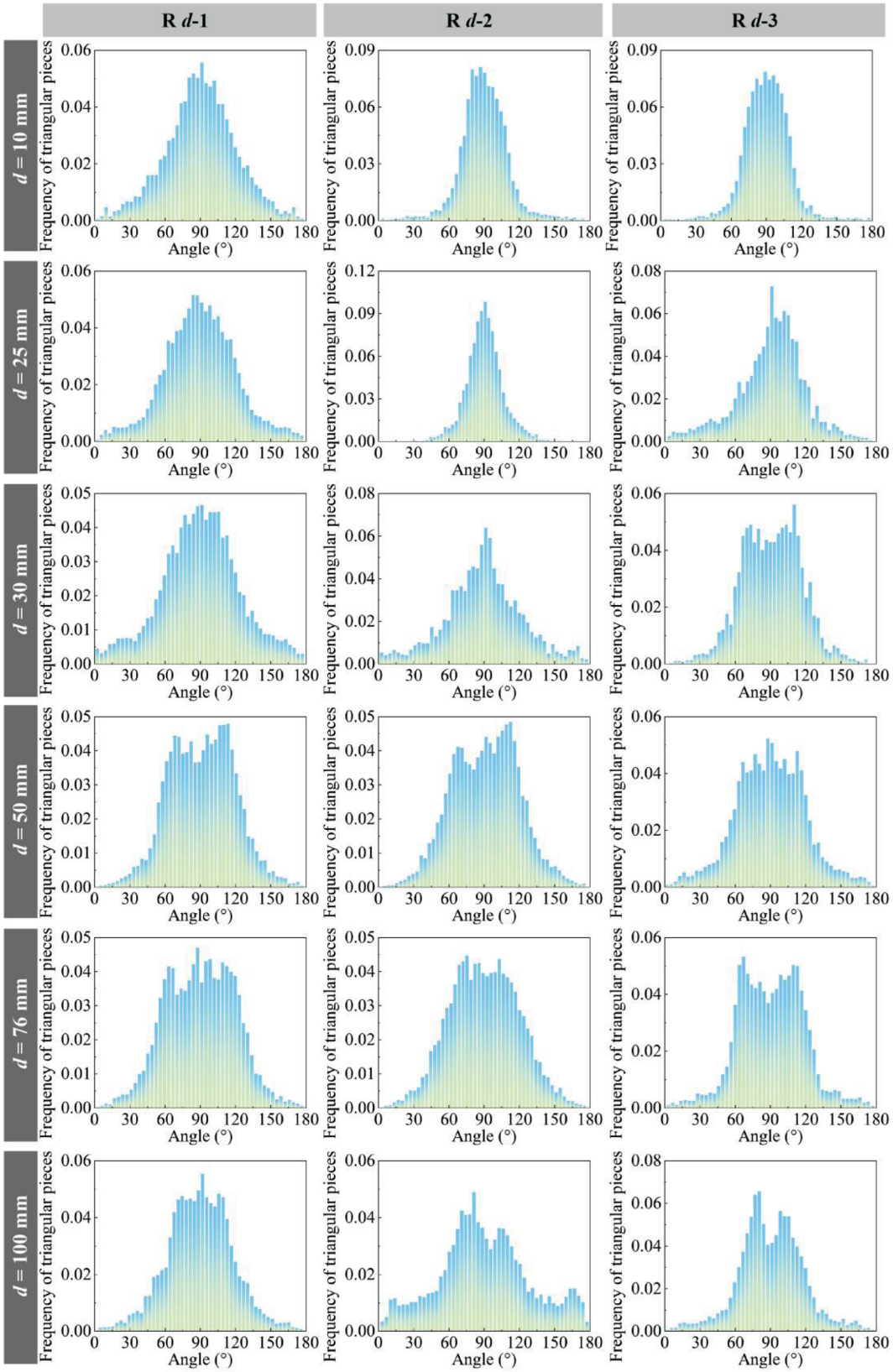

Fig. 14. Frequency distribution of crack angles.

the average 3D fractal dimension is approximately 2.09, suggesting relatively low geometric complexity of the cracks at this size. As the sample diameter increases, the fractal dimension gradually rises, reflecting an increase in the complexity of the crack structures. The fractal dimension reaches its peak at around 2.25 for a sample diameter of 76 mm, suggesting the highest geometric

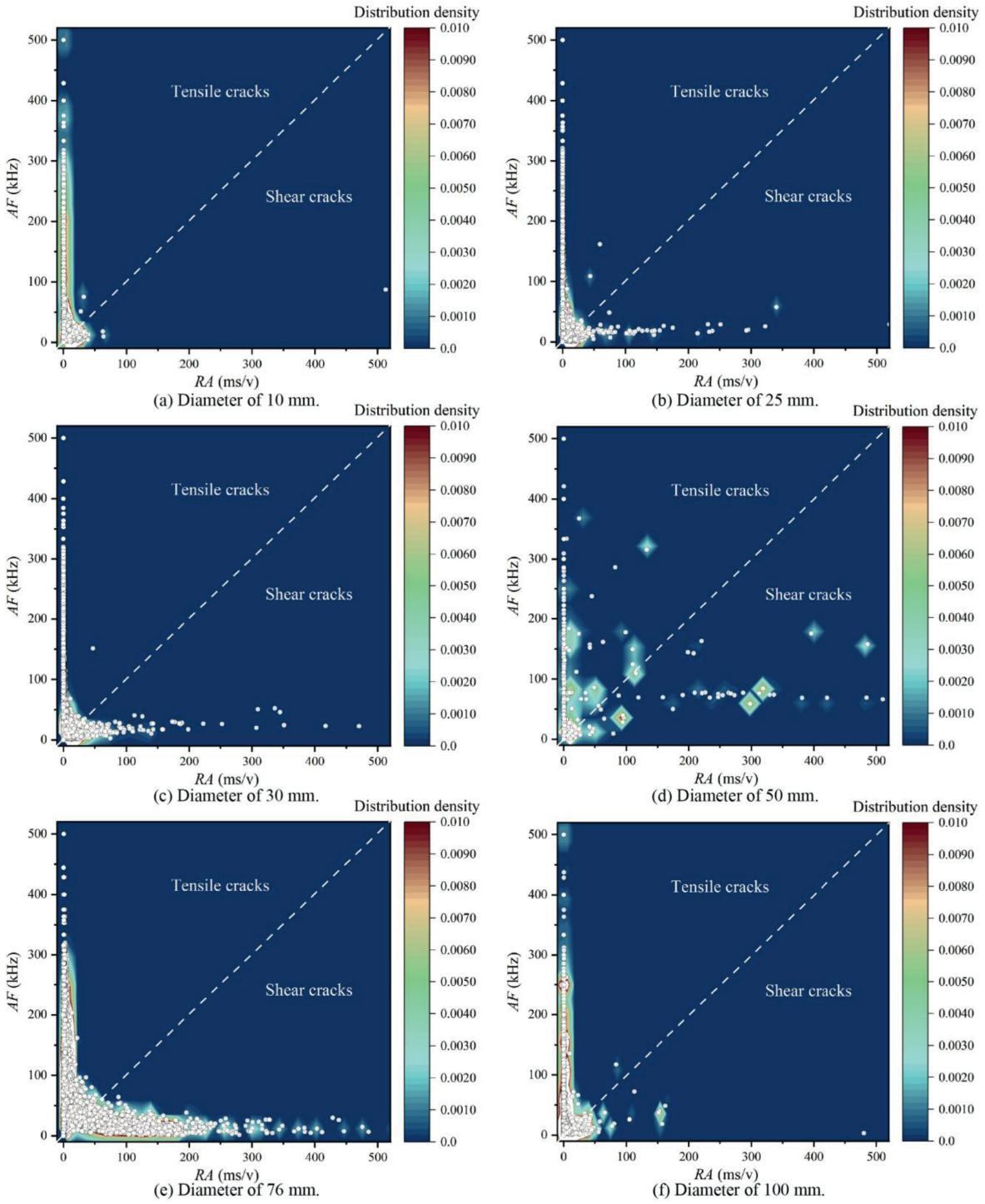

Fig. 15. Density distribution of acoustic emission (AE) parameters: rise angle (*RA*) and average frequency (*AF*). (a) Sandstone sample with a diameter of 10 mm, (b) Sandstone sample with a diameter of 25 mm, (c) Sandstone sample with a diameter of 30 mm, (d) Sandstone sample with a diameter of 50 mm, (e) Sandstone sample with a diameter of 76 mm, and (f) Sandstone sample with a diameter of 100 mm. The white dashed line separates tensile cracks from shear cracks.

complexity of cracks at this size. However, as the sample diameter increases to 100 mm, the fractal dimension slightly decreases, indicating a reduction in the complexity of the crack structure at larger sample sizes. Therefore, the fractal dimension can reflect the complexity of cracks, and its trend is consistent with that of UCS, showing an increase followed by a decrease as the specimen size increases.

4.2.4. Fragmentation degree

The distribution and characteristics of crack fragments are the key indicators for assessing material brittleness and strength (Reches, 1999; Tarasov and Potvin, 2013). Fig. 17 shows the volume and 3D spatial distribution of crack fragments in specimens of different sizes. For specimens with diameters of 10 mm and 25 mm, the number of fragments is relatively small, and their

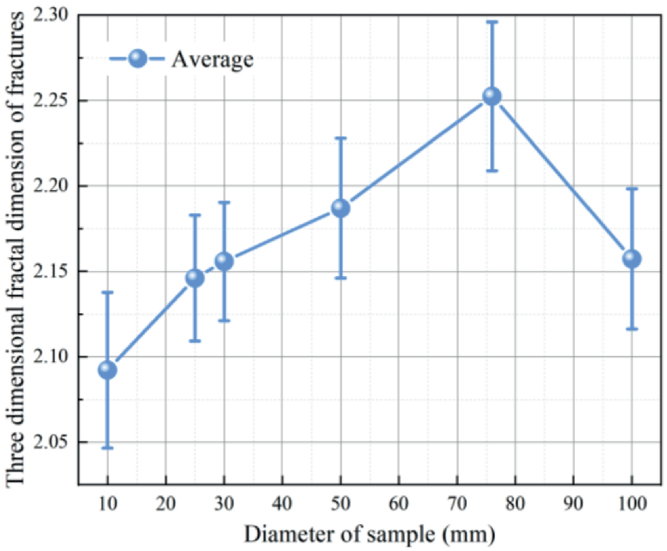

Fig. 16. Average values of the 3D fractal dimension of cracks.

volumes are minor, with fragments concentrated in the failure region. As the specimen diameter increases to 30 mm, 50 mm, and 76 mm, both the number and volume of fragments increase, and their distribution becomes more dispersed. The crack propagation paths are relatively longer, particularly in the 76 mm specimen, which exhibits more pronounced fragmentation characteristics. In contrast, for the 100 mm specimen, while the number of fragments decreases, their volumes increase significantly, and the fragments are more prominently distributed along the bedding planes. This indicates that the bedding structure plays a guiding role in crack propagation. To quantify the fragmentation degree of cracks, this study proposes a new fragmentation degree I to describe the combined effects of fragment number density and the average fragment volume ratio. The specific calculation formulas are as follows:

$$I = D \times \frac{1}{R} \tag{12}$$

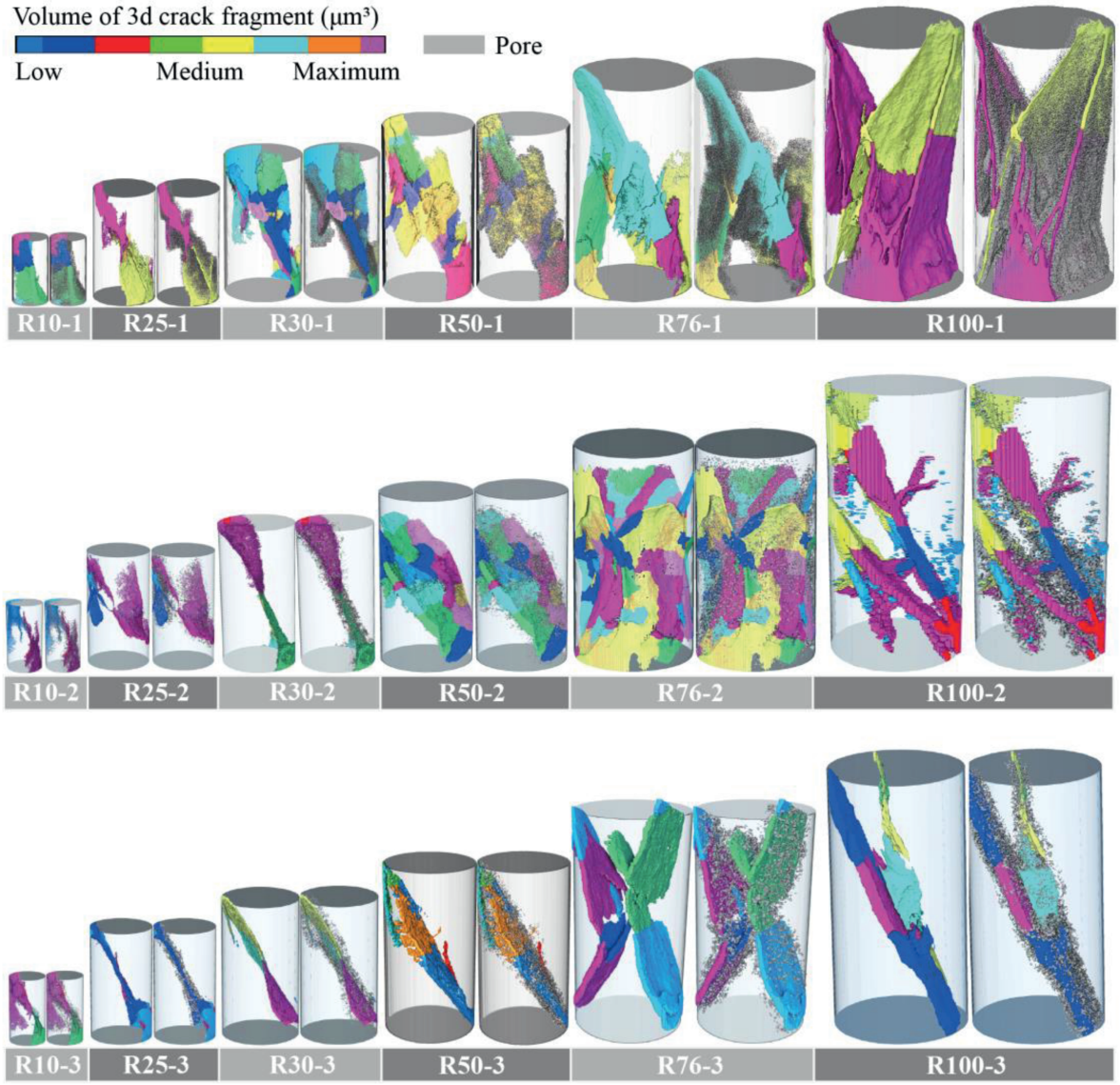

Fig. 17. Visualization of crack fragments for specimens of different sizes. 3D representation of crack fragments (left) and pore distribution in regions surrounding cracks (right).

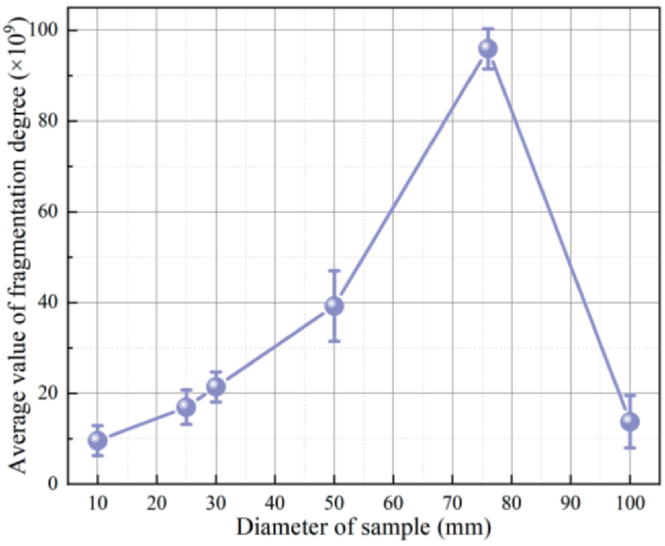

Fig. 18. Average fragmentation degree of cracks for specimens of different sizes.

$$D = \frac{N}{V_{\text{sample}}} \tag{13}$$

$$R = \frac{\overline{V}_{\text{fragment}}}{V_{\text{sample}}} \tag{14}$$

where D represents the fragment number density, i.e. the number of fragments per unit volume; N is the total number of fragments; and V_{sample} is the specimen volume. R represents the average fragment volume ratio, i.e. the ratio of the average fragment volume $\overline{V}_{\text{fragment}}$ to the specimen volume.

The fragmentation degree I combines the number and volume factors of fragments. Physically, an increase in fragment number density D reflects the generation of more fragments during the failure process, indicating a higher degree of fragmentation. Simultaneously, the reciprocal of the average fragment volume ratio $\frac{1}{R}$ reflects the relative size of fragments. A larger value indicates that fragments within the specimen are generally smaller and more densely distributed, further signifying a higher degree of fragmentation. Based on the results presented in Fig. 17, the fragmentation degree of specimens of different sizes was calculated, as shown in Fig. 18.

From Fig. 18, it can be observed that as the specimen diameter increases from 10 mm to 76 mm, the fragmentation degree rises sharply from 9.57×10^9 to 95.93×10^9, marking a 902.4 % increase. This suggests that fragmentation reaches its peak at 76 mm, indicating a maximum in crack propagation and fracture intensity. However, as the specimen diameter further increases to 100 mm, the fragmentation degree drops significantly to 13.73×10^9, reflecting an 85.69 % decline, which corresponds to a lower degree of fragmentation at this size. This trend suggests that as fracture fragmentation increases, the roughness of fracture surfaces becomes more pronounced, leading to enhanced frictional sliding. The increased friction promotes greater energy dissipation, making the rock failure process more gradual and progressive. Consequently, this transition contributes to higher rock strength, as suggested by Reches (1999) and Tarasov and Potvin (2013). The

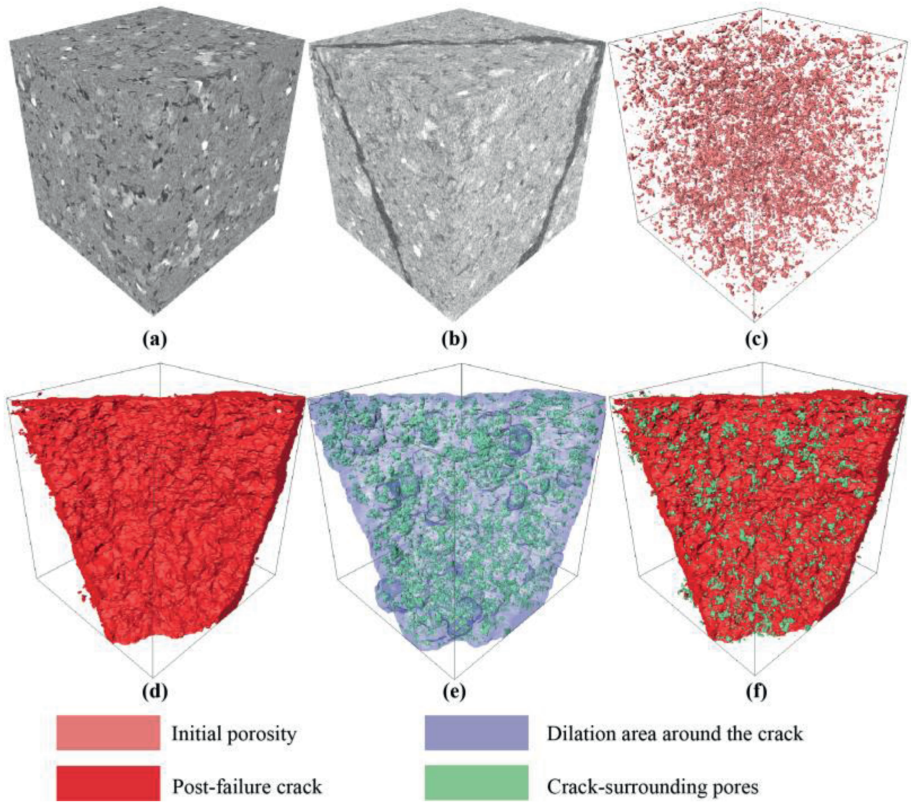

Fig. 19. Illustration of pore extraction near the crack region. (a) 3D reconstruction of CT data before fracturing, (b) 3D reconstruction of CT data after fracturing, (c) 3D reconstruction of pores before fracturing, (d) 3D reconstruction of cracks after fracturing, (e) Intersection of the crack expansion region and the initial pores, and (f) 3D visualization of cracks and intersecting pores.

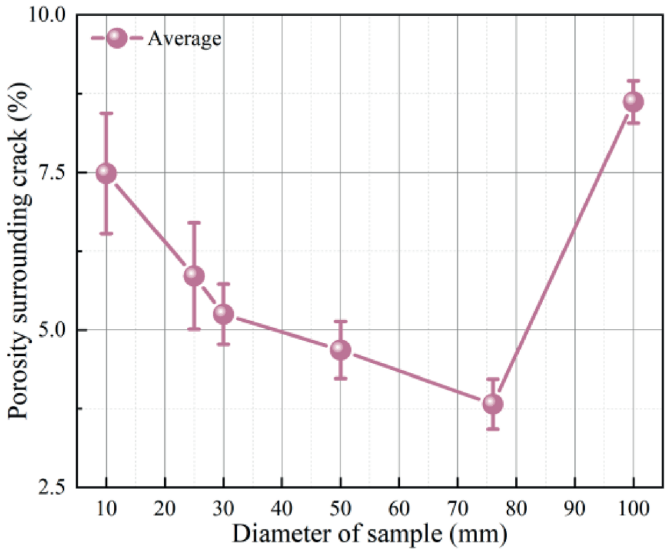

Fig. 20. Average porosity of pores surrounding cracks.

average fragmentation degree of cracks reflects the degree of fragmentation, which influences the roughness of fracture surfaces, leading to increased friction and energy dissipation. The fragmentation degree follows a trend consistent with UCS, increasing initially and then decreasing as the specimen size increases.

4.2.5. Relationship between fracture propagation and adjacent pores

For porous materials, the pore structure largely determines the crack propagation paths and failure modes (Hamdi et al., 2015; Zhao, 2021). However, using only the total porosity of the sample to characterize the effect of pore structure on crack propagation behavior has certain limitations. The total porosity of a sample reflects the overall pore distribution but fails to reveal the role of pores near cracks during the propagation process. Therefore, to accurately characterize the interaction mechanism between pores and cracks in sandstone specimens, detailed analysis of pore distribution around cracks was conducted based on CT 3D reconstruction data before and after fracturing. Using a cubic region of 2 mm × 2 mm × 2 mm as an example, the specific steps for data extraction are outlined below:

(1) CT Scanning and 3D reconstruction: CT scans of the specimens were performed before and after fracturing, yielding 3D reconstructed images of their internal structures. Fig. 19a and b displays the 3D reconstruction results before and after fracturing, respectively.
(2) Extraction of pore structure: The initial pore structure in Fig. 19a is extracted using a threshold segmentation method and reconstructed in 3D, as shown in Fig. 19c.
(3) Extraction of crack structure: Similarly, the crack structure in Fig. 19b is extracted via threshold segmentation, and its 3D reconstruction is displayed in Fig. 19d.
(4) Generation of crack expansion region: To identify the overlap between the crack region and the initial pores, the crack region was expanded outward by 10 pixels to generate an expansion region. Subsequently, the overlapping portion between the expansion region and the initial pores (Fig. 19c) is extracted, as shown in Fig. 19e.
(5) 3D Visualization of cracks and surrounding pores: The post-fracture cracks and the overlapping pores are combined and visualized in 3D, as illustrated in Fig. 19f.

Based on the above methodology, pore distribution results in the crack-adjacent regions for different sample sizes are obtained, as shown in Fig. 17. To further quantify the characteristics of pores surrounding the cracks, the crack-adjacent pore ratio for each sample i was calculated using:

$$P_i^{3d} = \frac{V_{pore,i}}{V_{region,i}} \tag{15}$$

where $V_{pore,i}$ represents the initial pore volume within the crack expansion region, and $V_{region,i}$ denotes the total volume of the crack expansion region. The crack-adjacent pore ratio P_i^{3d} reflects the pore density near the cracks for sample.

Using eq. (15), the average porosity surrounding cracks for samples of different sizes is obtained, as shown in Fig. 20. From the figure, it shows that as the sample diameter increases from 10 mm to 76 mm, the average porosity surrounding cracks decreases significantly. Smaller samples exhibit higher initial porosity, indicating stronger heterogeneity in pore distribution. This phenomenon may be due to the greater heterogeneity of initial pores in smaller samples, causing cracks to propagate along the weak areas where pores are concentrated. As the sample diameter increases to 76 mm, the pore distribution becomes more uniform, heterogeneity decreases, and crack propagation is constrained, thereby improving the rock's mechanical properties. When the sample size further increases to 100 mm, the bedding structure causes the pore space distribution to become more uneven, and cracks tend to propagate along the bedding planes, leading to a significant increase in the porosity around the cracks. In other words, the average porosity of pores surrounding cracks reflects the distribution and heterogeneity of pore space during the crack propagation process. Smaller samples have higher pore ratios, medium-sized samples exhibit more uniform pore distribution, while larger samples show increased pore ratios due to the impact of bedding structures.

5. Reverse size effect

The progressive failure of rock essentially involves the continuous development of internal microcracks (Martin, 1993; Walton, 2019). In brittle rocks, cohesion and friction are the two key strength components, and play critical roles during fracturing (Martin and Chandler, 1994; Zhao and Cai, 2010; David, 2012). However, cohesion and friction are not simultaneously mobilized throughout the process; instead, their activation is governed by crack evolution (Martin and Chandler, 1994; Zhao and Cai, 2010; David, 2012). Typically, at the crack initiation stage, tensile cracks dominate, leading to the progressive consumption of cohesion. Frictional strength is only mobilized when the cracks propagate and meet the conditions for frictional sliding (Hajiabdolmajid et al., 2002; Hajiabdolmajid and Kaiser, 2003; Zhao and Cai, 2010; Rafiei Renani and Martin, 2018a, 2018b). Based on the findings in Section 3, it can be inferred that the failure mechanism of red sandstone varies with sample size and can be categorized into three regions: small, medium, and large regions (Fig. 21d). Each region reveals how cohesion and friction alternately dominate the mechanical behavior of the samples under different fracture paths, crack propagation mechanisms, and energy dissipation modes.

For small-sized samples, the fracture process is influenced by

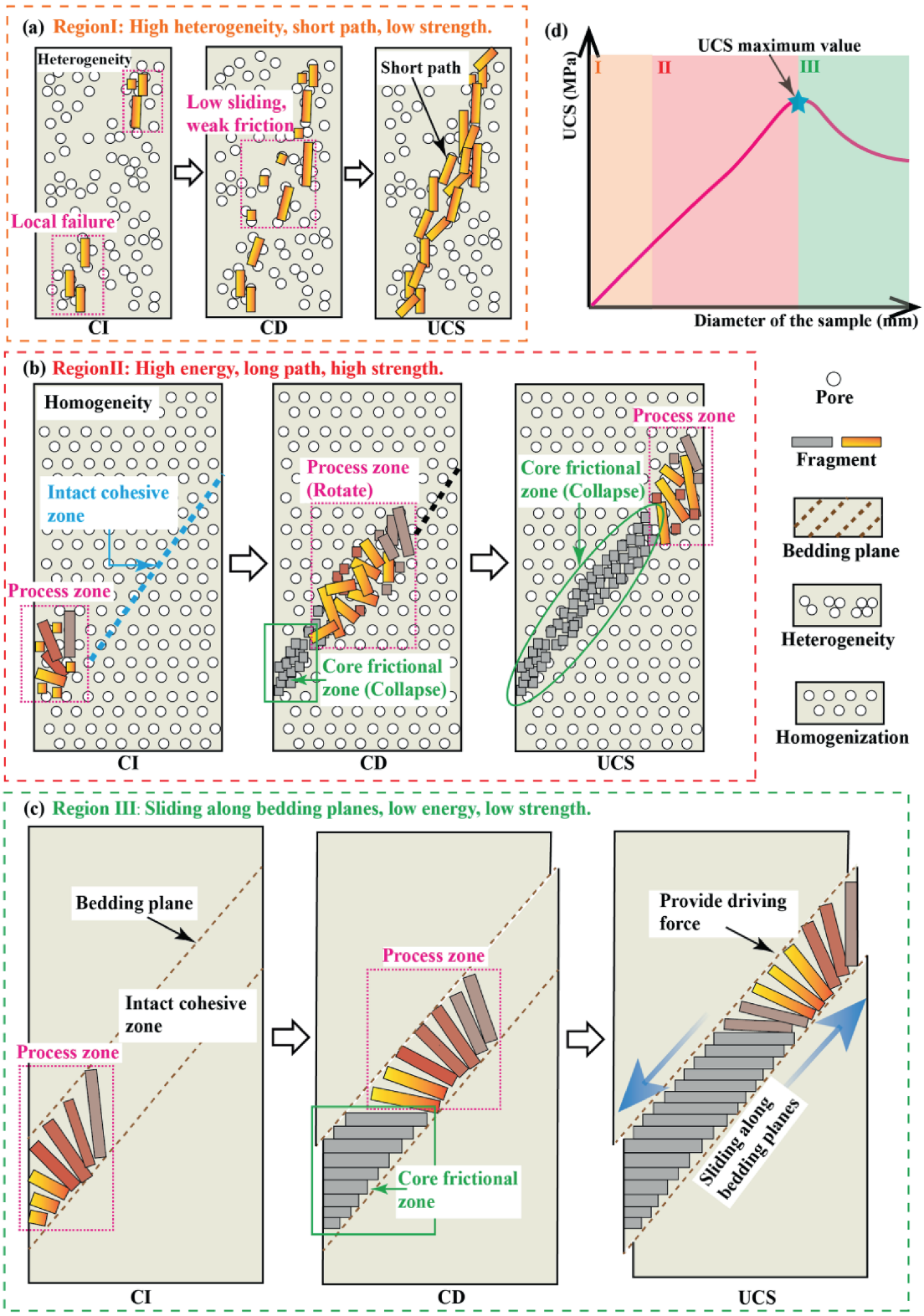

Fig. 21. Mechanism diagram of the reverse size effect on the rock compressive strength. (a) Sample representing the rising stage of the size effect, (b) Sample representing the inflection point of the size effect, and (c) Sample representing the decreasing stage of the size effect. (d) Ascending-descending type size effect curve.

the pore heterogeneity (Figs. 11 and 12). The internal pore distribution of the samples is highly uneven, leading to localized stress concentration under external loading. As the load increases, cracks propagate in regions of high stress concentration and quickly form through-cracks along shorter paths (Fig. 21a). As shown in Fig. 8, the normalized crack initiation stress and normalized damage stress of small-sized samples are relatively high. However, a higher normalized crack initiation stress does not necessarily indicate

increased rock strength; rather, it suggests that the rock will fail rapidly after strain localization occurs. Meanwhile, a higher normalized damage stress indicates a reduced likelihood of sliding along inclined planes, which is a critical condition for frictional strength mobilization (Martin and Chandler, 1994; Hajiabdolmajid et al., 2002; Lan et al., 2013; Liu et al., 2023). Consequently, it can be inferred that the frictional strength of small-sized samples is not fully mobilized, and tensile splitting failure plays a dominant role in the fracture process (Fig. 14), resulting in relatively low sample strength.

For medium-sized specimens (e.g. 76 mm), the influence of pore heterogeneity gradually diminishes (Fig. 12), resulting in a more tortuous crack propagation path (Fig. 11). During the crack initiation stage, stress is primarily concentrated on structurally weak regions, leading to the formation of an initial fracture process zone (Fig. 21b). A uniform pore distribution reduces local stress concentration effects, promoting a more dispersed crack initiation process. The lower normalized crack initiation stress (CI/UCS) (Fig. 8) suggests that the crack propagation mode tends toward a progressive evolution rather than abrupt failure (Martin and Chandler, 1994; Hajiabdolmajid et al., 2002; Lan et al., 2013; Liu et al., 2023). As the external load continues to increase, cracks propagate further, with stress concentration at the crack tips gradually inducing the separation of the sandstone matrix. During this process, cohesive strength progressively diminishes, and crack propagation transitions toward a friction-dominated stage, exhibiting more pronounced fragmentation characteristics (Fig. 18). The lower normalized damage stress (CD/UCS) observed in Fig. 8 indicates that frictional strength plays a crucial mobilizing role in this process (Martin and Chandler, 1994; Hajiabdolmajid et al., 2002; Lan et al., 2013; Liu et al., 2023). At this stage, frictional forces primarily govern crack propagation, leading to the rotation and relative movement of internal fragments within the specimen, which in turn increases the fractal dimension of the cracks (Fig. 16). The rotation of fragments not only extends the crack propagation path and enhances energy dissipation but also improves resistance to shear forces (Reches, 1999; Tarasov and Potvin, 2013). This process continues until the crack fully traverses the specimen, ultimately forming a macroscopic fracture (Fig. 17). In the final stage of failure, frictional resistance gradually replaces cohesive strength as the dominant failure mechanism, further dissipating energy and making shear failure the primary fracture mode. Consequently, this transition enhances the overall strength of medium-sized specimens.

For large-sized samples (e.g. 100 mm), although the crack propagation path is longer, the bedding structure predominantly dictates the crack trajectory (Fig. 11). During the crack initiation stress stage, cracks preferentially form initial slip paths along the bedding planes (Si et al., 2021). Since the slip region remains within the cohesive strength-controlled zone, the integrity of the bedding plane structure is relatively preserved. As the external load increases to the damage stress stage, cracks are influenced by frictional resistance and gradually slip along the bedding planes. During this process, the bedding planes guide the crack propagation path, and cracks no longer propagate in a complex, rotational manner. Instead, they slide along the bedding planes, progressively expanding the fracture zone. When the stress reaches its peak, cracks fully propagate along the bedding planes, forming macroscopic fractures (Fig. 21c). Compared to the rotational fragmentation mode observed in medium-sized samples, this slip-dominated fracture mode achieves through-sample fracturing with relatively lower energy consumption (Reches, 1999; Tarasov and Potvin, 2013). Crack propagation in this mode no longer requires overcoming significant cohesive and frictional forces, resulting in reduced energy consumption and consequently lower sample strength.

6. Conclusions

This study investigates the reverse size effect in red sandstone through unconfined compression tests and high-resolution CT scanning. The main conclusions are as follows:

(1) Macroscopic parameters: Crack initiation stress (CI), damage stress (CD), and UCS increase and then decrease with specimen size, while normalized CI and CD initially decrease and then increase. The elastic modulus increases with size, while the Poisson's ratio fluctuates.
(2) Pore and crack failure morphology: As the specimen size increases, the entropy of pore heterogeneity, fractal dimension, and fragmentation degree follow the same trend as UCS, first increasing and then decreasing, while the porosity surrounding cracks shows the opposite trend. The failure morphology transitions from localized splitting to shear failure, ultimately evolving into a tensile-shear composite failure along the bedding plane.
(3) Controlling mechanisms: In small specimens, stress concentration leads to splitting failure and lower strength. In medium-sized specimens, friction governs crack propagation, leading to shear failure and high strength. In large specimens, bedding effects guide crack propagation along planes, reducing energy dissipation and strength.
(4) The proposed quantitative indicators, including 3D crack angle statistics, fractal dimension, comprehensive fragmentation degree, and the porosity around cracks, provide valuable insights for analyzing the influence of pore structure and crack evolution on the mechanical behavior of rocks.

CRediT authorship contribution statement

Qinyuan Liang: Writing – original draft, Validation, Methodology, Visualization, Software, Investigation, Data curation, Formal analysis, Conceptualization. **Hengxing Lan:** Validation, Resources, Funding acquisition, Data curation, Writing – review & editing, Supervision, Project administration, Formal analysis, Conceptualization. **Yu Zhou:** Visualization, Methodology, Formal analysis, Conceptualization, Writing – review & editing, Validation, Investigation, Data curation. **Bo Li:** Visualization, Software, Methodology, Funding acquisition, Conceptualization, Writing – review & editing, Validation, Resources, Investigation, Data curation. **Shijie Liu:** Writing – review & editing, Visualization, Investigation, Conceptualization, Validation, Formal analysis. **Han Bao:** Writing – review & editing, Investigation, Validation, Formal analysis.

Declaration of competing interest

The authors declare that they have no known competing financial interests or personal relationships that could have appeared to influence the work reported in this paper.

Acknowledgments

The authors greatly acknowledge the financial support from the National Natural Science Foundation of China (Grant No. 42041006), and the Fundamental Research Funds for the Central Universities, CHD (Grant Nos. 300102265718, 300102264902).

References

Aggelis, D., 2011. Classification of cracking mode in concrete by acoustic emission parameters. Mech. Res. Commun. 38 (3), 153–157.

Ban, L., Du, W., Zheng, D., Hou, Y., Qi, C., Yu, J., Zhu, C., Lu, C., 2024. Velocity-dependent effect on the peak shear strength of rock joints considering the distribution characteristics of contact joint surface. Rock Mech. Rock Eng. 57, 2523–2537.

Bao, H., Zhang, G., Lan, H., Yan, C., Xu, J., Xu, W., 2020. Geometrical heterogeneity of the joint roughness coefficient revealed by 3D laser scanning. Eng. Geol. 265, 105415.

Barton, N., Wang, C., Yong, R., 2023. Advances in joint roughness coefficient (JRC) and its engineering applications. J. Rock Mech. Geotech. Eng. 15 (12), 3352–3379.

Bažant, Z., 1984. Size effect in blunt fracture: concrete, rock, metal. J. Eng. Mech. 110, 518–535.

Bažant, Z., 1997. Scaling of quasibrittle fracture: hypotheses of invasive and lacunar fractality, their critique and weibull connection. Int. J. Fract. 83, 41–65.

Bieniawski, Z., 1968. The effect of specimen size on compressive strength of coal. Int. J. Rock Mech. Min. Sci. Geomech. Abstr. 5, 325–335.

Carpinteri, A., Chiaia, B., Ferro, G., 1995. Size effects on nominal tensile strength of concrete structures: multifractality of material ligaments and dimensional transition from order to disorder. Mater. Struct. 28, 311–317.

Chen, J., Lan, H., Macciotta, R., Wu, Y., Li, Q., Zhao, X., 2018. Anisotropy rather than transverse isotropy in Longmaxi shale and the potential role of tectonic stress. Eng. Geol. 247, 38–47.

Cheng, X., Tian, W., Gao, J., Guo, J., Wang, X., 2022. Grey entropy analysis of strength and void structure of carbon nanotubes concrete under the coupling of sulfate attack and freeze-thaw cycles. Constr. Build. Mater. 358, 129462.

Cuisiat, F., Haimson, B., 1992. Scale effects in rock mass stress measurements. Int. J. Rock Mech. Min. Sci. Geomech. Abstr. 29, 99–117.

Darlington, W., Ranjith, P., Choi, S., 2011. The effect of specimen size on strength and other properties in laboratory testing of rock and rock-like cementitious brittle materials. Rock Mech. Rock Eng. 44, 513–529.

David, O., 2012. Application of a transversely isotropic brittle rock mass model in roof support design. Int. J. Min. Sci. Technol. 22, 639–643.

González-Fernández, M., Estévez-Ventosa, X., Alejano, L., Masoumi, H., 2023. Size-dependent behaviour of hard rock under triaxial loading. Rock Mech. Rock Eng. 56, 6009–6025.

González-Fernández, M., Estévez-Ventosa, X., Pérez-Rey, I., Alejano, L., Masoumi, H., 2024. Size effects on strength and deformability of artificially jointed hard rock. Int. J. Rock Mech. Min. Sci. 176, 105696.

Hajiabdolmajid, V., Kaiser, P., Martin, C., 2002. Modelling brittle failure of rock. Int. J. Rock Mech. Min. Sci. 39, 731–741.

Hajiabdolmajid, V., Kaiser, P., 2003. Brittleness of rock and stability assessment in hard rock tunneling. Tunn. Undergr. Space Technol. 18 (1), 35–48.

Hamdi, P., Stead, D., Elmo, D., 2015. Characterizing the influence of stress-induced microcracks on the laboratory strength and fracture development in brittle rocks using a finite-discrete element method-micro discrete fracture network FDEM-μDFN approach. J. Rock Mech. Geotech. Eng. 7, 609–625.

Han, G., Liang, Q., Bao, R., Zhou, Y., 2022. Influence of circular hole diameter on deformation and failure of Longmaxi shale. Geotech. Geol. Eng. 40 (5), 2605–2613.

Han, Z., Zhang, Y., Zhang, W., Qiao, H., Feng, Q., Xue, C., Shang, M., 2023. Study on comprehensive morphological parameters of manufactured sand based on CT scanning and entropy method and its application in rheology of manufactured sand mortar. Constr. Build. Mater. 370, 130628.

Hawkins, A., 1998. Aspects of rock strength. Bull. Eng. Geol. Environ. 57, 17–30.

He, S., Li, M., Shi, S., Lu, Y., Wang, D., 2024. Experimental study on the influence of rock pore structure on pressure stimulated voltage variations based on nuclear magnetic resonance. Eng. Geol. 341, 107736.

Hecht, C., Bönsch, C., Bauch, E., 2005. Relations of rock structure and composition to petrophysical and geomechanical rock properties: examples from permo-carboniferous red-beds. Rock Mech. Rock Eng. 38, 197–216.

Hoskins, J., Horino, F., 1969. Influence of spherical head size and specimen diameters on the uniaxial compressive strength of rocks. Rep. Invest. 7234. U.S. Department of the Interior, Bureau of Mines.

Huang, B., Li, L., Tan, Y., Hu, R., Li, X., 2020. Investigating the meso-mechanical anisotropy and fracture surface roughness of continental shale. JGR Solid Earth 125, e2019JB017828.

ISRM, 1979. Suggested methods for determining the uniaxial compressive strength and deformability of rock materials. Int. J. Rock Mech. Min. Sci. Geomech. Abstr. 16 (3), 195–214.

Jamshidi, A., Nikudel, M., Khamehchiyan, M., Sahamieh, R., 2016. The effect of specimen diameter size on uniaxial compressive strength, P-wave velocity and the correlation between them. Geomechanics Geoengin. 11 (1), 13–19.

Ju, Y., Yang, Y., Peng, R., Mao, L., 2013. Effects of pore structures on static mechanical properties of sandstone. J. Geotech. Geoenviron. Eng. 139, 1745–1755.

Karakas, A., 2008. Practical rock engineering. Environ. Eng. Geosci. 14, 55–57.

Lan, H., Chen, J., Macciotta, R., 2019. Universal confined tensile strength of intact rock. Sci. Rep. 9, 6170.

Lan, H., Martin, C., Andersson, J., 2013. Evolution of in situ rock mass damage induced by mechanical–thermal loading. Rock Mech. Rock Eng. 46, 153–168.

Lan, H., Martin, C., Hu, B., 2010. Effect of heterogeneity of brittle rock on micromechanical extensile behavior during compression loading. J. Geophys. Res. 115, B01202.

Li, K., Cheng, Y., Fan, X., 2018. Roles of model size and particle size distribution on macro-mechanical properties of Lac du Bonnet granite using flat-joint model. Comput. Geotech. 103, 43–60.

Li, L., Tan, Y., Huang, B., Deng, X., 2020. Pore property as an indicator of macro-deterioration in slightly weathered tuffs. Eng. Geol. 267, 105492.

Liang, Q., Lan, H., Zhou, Y., Li, B., Sun, W., Liu, S., Lv, W., 2025. Reverse size effect of the unconfined compressive strength of crystalline rock: a grain-scale perspective. Rock Mech. Rock Eng. 58 (2), 1651–1669.

Liang, Q., Zhao, C., Zhou, Y., Li, B., Bao, R., 2022. Investigation on the deformation and failure characteristics of shale samples containing circular hole considering the bedding angle effect under uniaxial compression. Math. Probl Eng. 2022 (1), 7100444.

Liu, J., Wang, Y., Zhang, X., Rong, J., 2016. Early Telychian (Silurian) marine siliciclastic red beds in the Eastern Yangtze Platform, South China: distribution pattern and controlling factors. Can. J. Earth Sci. 53 (7), 712–718.

Liu, S., Lan, H., Martin, C., 2023. Effect of disturbance on the progressive failure process of Eastern Himalayan Gneiss. Eng. Geol. 312, 106936.

Liu, S., Lan, H., Strom, A., Li, L., Bao, H., 2024. Spatial segmentation of Jiali Fault's Holocene activity in the southeastern Tibetan Plateau. npj Nat. Hazards 1 (1), 1–12.

Liu, S., Lan, H., Chen, Z., Li, L., Bao, H., 2025a. Biotite effect on the anisotropic properties of gneiss in Eastern Himalayas, China. J. Rock Mech. Geotech. Eng. S1674775525001489.

Liu, S., Lan, H., Chen, H., Huang, X., Li, L., Han, B., 2025b. Differences in the failure process of grottoes sandstone in southern and northern China determined by microstructure. npj Herit. Sci. 13 (1), 1–16.

Martin, C., 1993. The Strength of Massive Lac Du Bonnet Granite Around Underground Openings. PhD Thesis. University of Manitoba, Manitoba, Canada.

Martin, C., Chandler, N., 1994. The progressive fracture of Lac du Bonnet granite. Int. J. Rock Mech. Min. Sci. Geomech. Abstr. 31 (6), 643–659.

Masoumi, H., 2013. Investigation into the Mechanical Behaviour of Intact Rock at Different Sizes. University of New South Wales (UNSW), Sydney, Australia. PhD Thesis.

Masoumi, H., Saydam, S., Hagan, P., 2016. Unified size-effect law for intact rock. Int. J. GeoMech. 16, 04015059.

McClay, K., Norton, M., Coney, P., Davis, G., 1986. Collapse of the caledonian orogen and the old red sandstone. Nature 323 (6084), 147–149.

Miščević, P., Vlastelica, G., 2019. Estimation of embankment settlement caused by deterioration of soft rock grains. Bull. Eng. Geol. Environ. 78, 1843–1853.

Nicksiar, M., Martin, C., 2014. Factors affecting crack initiation in low porosity crystalline rocks. Rock Mech. Rock Eng. 47, 1165–1181.

Ohno, K., Ohtsu, M., 2010. Crack classification in concrete based on acoustic emission. Constr. Build. Mater. 24 (12), 2339–2346.

Peng, J., Wong, L., Teh, C., 2017. Influence of grain size heterogeneity on strength and microcracking behavior of crystalline rocks. JGR Solid Earth 122, 1054–1073.

Qi, S., Lan, H., Martin, C., Huang, X., 2020. Factors controlling the difference in Brazilian and direct tensile strengths of the Lac du Bonnet granite. Rock Mech. Rock Eng. 53, 1005–1019.

Qiao, L., Wu, F., Zhou, X., Chen, Y., Zhang, Y., 2024. Research on point load correction factor based on electro-hydraulic servo point load meter. Rock Mech. Rock Eng. 57 (8), 5705–5725.

Quiñones, J., Arzúa, J., Alejano, L., García-Bastante, F., Mas Ivars, D., Walton, G., 2017. Analysis of size effects on the geomechanical parameters of intact granite samples under unconfined conditions. Acta Geotech 12, 1229–1242.

Rafiei Renani, H., Martin, C., 2018a. Modeling the progressive failure of hard rock pillars. Tunn. Undergr. Space Technol. 74, 71–81.

Rafiei Renani, H., Martin, C., 2018b. Cohesion degradation and friction mobilization in brittle failure of rocks. Int. J. Rock Mech. Min. Sci. 106, 1–13.

Rahner, M., Halisch, M., Fernandes, C., Weller, A., dos Santos, V., 2018. Fractal dimensions of pore spaces in unconventional reservoir rocks using X-ray nano- and micro-computed tomography. J. Nat. Gas Sci. Eng. 55, 298–311.

Ramsey, J., Chester, F., 2004. Hybrid fracture and the transition from extension fracture to shear fracture. Nature 428, 63–66.

Reches, Z., 1999. Mechanisms of slip nucleation during earthquakes. Earth Planet Sci. Lett. 170 (4), 475–486.

Rong, J., Wang, Y., Zhang, X., 2012. Tracking shallow marine red beds through geological time as exemplified by the lower Telychian (Silurian) in the Upper Yangtze Region, South China. Sci. China Earth Sci. 55, 699–713.

Russell, D., Hanson, J., Ott, E., 1980. Dimension of strange attractors. Phys. Rev. Lett. 45 (14), 1175.

Shiotani, T., Ohtsu, M., Ikeda, K., 2001. Detection and evaluation of AE waves due to rock deformation. Constr. Build. Mater. 15 (5–6), 235–246.

Si, X., Huang, L., Li, X., Ma, C., Gong, F., 2021. Experimental investigation of spalling failure of D-shaped tunnel under three-dimensional high-stress conditions in hard rock. Rock Mech. Rock Eng. 54, 3017–3038.

Song, H., Jiang, Y., Elsworth, D., Zhao, Y., Wang, J., Liu, B., 2018. Scale effects and strength anisotropy in coal. Int. J. Coal Geol. 195, 37–46.

Su, G., Chen, X., Sun, G., Chen, B., Zhao, G., 2023. Experimental study on the evolutionary characteristics of acoustic signals produced by granite damage under uniaxial compression. Int. J. Damage Mech. 32, 715–745.

Tarasov, B., Potvin, Y., 2013. Universal criteria for rock brittleness estimation under triaxial compression. Int. J. Rock Mech. Min. Sci. 59, 57–69.

Trümper, S., Gaitzsch, B., Schneider, J., Ehling, B.C., Kleeberg, R., Rößler, R., 2020. Late Palaeozoic red beds elucidate fluvial architectures preserving large woody debris in the seasonal tropics of central Pangaea. Sedimentology 67 (4), 1973–2012.
Walton, G., 2019. Initial guidelines for the selection of input parameters for cohesion-weakening-friction-strengthening (CWFS) analysis of excavations in brittle rock. Tunn. Undergr. Space Technol. 84, 189–200.
Wang, G., Shen, J., Liu, S., Jiang, C., Qin, X., 2019. Three-Dimensional Modeling and Analysis of macro-pore Structure of Coal Using Combined X-ray CT Imaging and Fractal Theory.
Wang, H., Liu, D., Cui, Z., Cheng, C., Jian, Z., 2016. Investigation of the fracture modes of red sandstone using XFEM and acoustic emissions. Theor. Appl. Fract. Mech. 85, 283–293.
Wang, S., Masoumi, H., Oh, J., Zhang, S., 2020. Scale-Size and Structural Effects of Rock Materials. Woodhead Publishing, pp. 24–27.
Weibull, W., 1939. A statistical theory of the strength of materials. Swed. R. Inst. Eng. Res. 151, 1–45.
Weibull, W., 1951. A statistical distribution function of wide applicability. J. Appl. Mech. 18 (3), 293–297.
Wu, F., Qiao, L., Guan, S., Zhang, Q., Wang, Z., Wu, J., 2021. Uniaxial compression test study on size effect of small rock samples. Chin. J. Rock Mech. Eng. 40, 865–873 (in Chinese).
Wu, K., Meng, Q., Li, R., Luo, L., Ke, Q., Wang, C., Ma, C., 2024. A machine learning-based strategy for predicting the mechanical strength of coral reef limestone using X-ray computed tomography. J. Rock Mech. Geotech. Eng. 7 (5), 2790–2800.
Xu, Q., Wang, X., Chen, J., 2020. Quantitative evaluation of pore-scale heterogeneity based on statistical analysis of a pore network model of unconsolidated porous media. Hydrogeol. J. 28, 1841–1852.
Yang, B., He, M., Wang, H., Zhang, Z., Zhu, J., Li, N., 2023. Experimental investigation on brittleness characteristics of rock based on the ubiquitiformal complexity: strain rate effect and size effect. Bull. Eng. Geol. Environ. 82 (8), 306.
Yang, S., Liu, X., Jing, H., 2013. Experimental investigation on fracture coalescence behavior of red sandstone containing two unparallel fissures under uniaxial compression. Int. J. Rock Mech. Min. Sci. 63, 82–92.
Yuan, X., Dai, M., Gao, Y., Liu, F., Zhang, M., 2023. Pore morphology based on graphene oxide modified steel fibre concrete for freeze–thaw resistance. Constr. Build. Mater. 409, 133877.
Yuki, N., Aoto, S., Ogata, Y., Yoshinaka, R., Terada, M., 1995. The scale and creep effects on strength of welded tuff. In: Rock Foundation, pp. 219–222.
Zhai, H., Masoumi, H., Zoorabadi, M., Canbulat, I., 2020. Size-dependent behaviour of weak intact rocks. Rock Mech. Rock Eng. 53, 3563–3587.
Zhang, G., Ling, S., Liao, Z., Xiao, C., Xu, X., 2024a. Mechanism and influence on red-bed soft rock disintegration durability of particle roughness based on experiment and fractal theory. Constr. Build. Mater. 419, 135504.
Zhang, X., Luo, X., He, X., Niu, S., 2024b. Pore structure expansion and evolution in sandstone with prefabricated crack under freeze-thaw cycles based on CT scanning. Front. Earth Sci. 12, 1394731.
Zhang, G., Ling, S., Wu, X., 2023. Evolution of disintegration breakage of Upper Cretaceous red-bed mudstone in an acidic environment based on the Weibull model. Acta Geotech 18, 6573–6593.
Zhang, M., Yin, Y., Huang, B., 2015. Mechanisms of rainfall-induced landslides in gently inclined red beds in the eastern Sichuan Basin, SW China. Landslides 12, 973–983.
Zhang, Q., Zhu, H., Zhang, L., Ding, X., 2011. Study of scale effect on intact rock strength using particle flow modeling. Int. J. Rock Mech. Min. Sci. 48, 1320–1328.
Zhang, Z., Jiang, Q., Zhou, C., Liu, X., 2014. Strength and failure characteristics of Jurassic red-bed sandstone under cyclic wetting–drying conditions. Geophys. J. Int. 198, 1034–1044.
Zhao, D., Xia, Y., Zhang, C., Liu, N., Tang, C., Singh, H., Chen, J., Wang, P., 2023a. A new method to investigate the size effect and anisotropy of mechanical properties of columnar jointed rock mass. Rock Mech. Rock Eng. 56, 2829–2859.
Zhao, Y., He, X., Jiang, L., Wang, Z., Ning, J., Sainoki, A., 2023b. Influence analysis of complex crack geometric parameters on mechanical properties of soft rock. Int. J. Coal Sci. Technol. 10 (1), 78.
Zhao, D., Xia, Y., Zhang, C., Tang, C., Zhou, H., Liu, N., Singh, H., Zhao, Z., Chen, J., Mu, C., 2022. Failure modes and excavation stability of large-scale columnar jointed rock masses containing interlayer shear weakness zones. Int. J. Rock Mech. Min. Sci. 159, 105222.
Zhao, X.G., Cai, M., 2010. Influence of plastic shear strain and confinement-dependent rock dilation on rock failure and displacement near an excavation boundary. Int. J. Rock Mech. Min. Sci. 47, 723–738.
Zhao, Y., 2021. Retrospection on the development of rock mass mechanics and the summary of some unsolved centennial problems. Chin. J. Rock Mech. Eng. 40 (7), 1297–1336 (in Chinese).
Zhou, Y., Feng, W., Hu, Y., Yi, X., Ji, F., Li, W., 2024. Equivalent continuous numerical simulation of a large-scale underground powerhouse excavation considering the size effect of the jointed rock mass. Tunn. Undergr. Space Technol. 154, 106058.
Zhou, Y., Lv, W., Li, B., Liang, Q., Wang, S., 2025a. A realistic 3D grain-based modeling approach for reproducing the mechanical and failure behavior of brittle granites. Int. J. Rock Mech. Min. Sci. 185, 105981.
Zhou, Z., Chen, H., Liang, Q., Wang, Q., Hao, J., Zhuang, S., 2025b. Multi-scale analysis of degradation mechanisms in magnesium phosphate cement paste under wet-dry cycling. Cem. Concr. Compos., 105939

Dr. Hengxing Lan is a professor at the Institute of Geographic Sciences and Natural Resources Research, Chinese Academy of Sciences (CAS), China. He is the President of the Landslide Nomenclature Commission (C37), International Association for Engineering Geology and the Environment (IAEG). He serves on the editorial board of high-profile journals in geology and geotechnical engineering. His research is primarily focused on the characterization and modeling of rock and soil strength and failure, with a particular emphasis on the microscopic anisotropic control theory of rock mass deformation and failure. He has published over 200 academic papers and 15 scientific consulting reports that have been adopted by the Chinese government. The geological hazard dynamics model he proposed has been successfully applied in academic and engineering communities of nearly 40 countries worldwide, and has been cited in research reports by the US Academy of Sciences.